Polymer 51 (2010) 5623–5639

Contents lists available at ScienceDirect

Polymer

journal homepage: www.elsevier.com/locate/polymer

# Frozen-in birefringence and anisotropic shrinkage in optical moldings: II. Comparison of simulations with experiments on light-guide plates

Avraam I. Isayev*, Tsui Hsun Lin, Keehae Kwon

*Department of Polymer Engineering, The University of Akron, Akron, OH 44325-0301, United States*

ARTICLE INFO

*Article history:*
Received 23 June 2010
Received in revised form
16 September 2010
Accepted 20 September 2010
Available online 26 September 2010

*Keywords:*
Numerical simulation
Injection molding
Birefringence

ABSTRACT

The thermally-, flow-induced and total birefringence components and anisotropic shrinkages in LGP moldings were simulated by using a combination of a CV/FEM/FDM technique nonlinear viscoelastic and photoviscoelastic constitutive equations and orientation functions, as described in Part I of this study. The simulated results were compared with measurements on LGP moldings of a polystyrene (PS) and two optical grade polycarbonates (PCs) OQ1030 and OQ3820 having low and high molecular weights. The thermally-induced birefringence was simulated by a combination of constrained and free cooling during molding. In LGP moldings of PS, the simulated thermally-induced birefringence indicated a minor variation with location in the mold plane, a parabolic shape in the core region and an increase towards the wall. Compared to the flow-induced birefringence, the thermal birefringence provided a minor contribution to the total transverse birefringence $\Delta n_{12}$. In LGP moldings of PCs, the simulated thermally-induced birefringence showed a significant variation with location in the mold plane, nearly constant value in the core region and high value in the wall region. In LGP moldings of both PCs, the contributions of the thermally- and flow-induced birefringence to the total transverse birefringence $\Delta n_{12}$ were significant. The effect of processing conditions on the development of the normal birefringence in LGP moldings of PCs was ranked from most to least: the packing pressure, mold temperature, melt temperature, injection speed and packing time. However, in LGP moldings of PS the packing time effect was significant due to a longer gate freezing time. Simulated and measured normal birefringence along the flow direction was in fair agreement, but simulations were unable to describe the observed birefringence maximum arising near the gate. The averaged luminance of LGP moldings exhibited some correlation with the averaged normal birefringence. LGP moldings of PC OQ1030 indicated a pronounced maximum in the simulated transverse flow birefringence in the core but a low value near the wall. In contrast, the LGP molding of PC OQ3820 showed a high simulated birefringence near the wall and a low value of maximum in the core. The simulated and measured total transverse birefringence in LGP moldings was in fair agreement. LGP molding of both PCs showed similar tendency in shrinkage variation with processing conditions. However, the thickness shrinkage was higher in LGP moldings of PC OQ3820. The effect of processing conditions on the development of shrinkage in LGP moldings of both PCs was ranked from most to least: the packing pressure, melt temperature, mold temperature, injection speed and packing time. In LGP moldings of PS, the thickness shrinkage slightly increased with increasing melt temperature and significantly increased with reducing packing time. A good agreement between the simulated and measured anisotropic shrinkages in LGP moldings at various processing conditions was observed.



## 1. Introduction

Injection molding is one of the most widely employed polymer processing methods, being characterized by high degree of automation, high productivity and good dimensional stability of moldings. Molding of precise plastic optical parts such as optical disks (CD or DVD substrates), micro-scale prisms (MSPs) and light-guide plates (LGPs) is an important technology in the industry today. Two recent books provide a general overview on this technology [1,2]. In comparison with conventional optical glass parts, plastics offer several significant advantages including light weight and low cost. An additional benefit of injection molding is the ability to make the products with complicated shapes, such as various fitted-joints that can be molded in a one-shot process. Typical materials used for manufacturing optical products are

* Corresponding author. Fax: +1 330 258 2339.
*E-mail address:* aisayev@uakron.edu (A.I. Isayev).

0032-3861/$ – see front matter © 2010 Elsevier Ltd. All rights reserved.
doi:10.1016/j.polymer.2010.09.055

polycarbonates (PCs), polymethylmethacrylates (PMMAs) and cyclic olefins (COCs). The major concern in the manufacturing of LGPs is the light transmission, termed luminance, because plastic LGP needs to deliver the light from its edges to the front surface with the highest possible efficiency. To obtain the highest luminance, Togaya et al. [3] developed a backlight system using a highly scattering optical transmission (HSOT) polymer having high optical quality. More recently, Okumura et al. [4] created a highly efficient HSOT backlight system not requiring optical sheets. This is not only improved optical performance, but also reduced the size of the entire backlight module. By changing the material of light-guide plate, Visser [5] applied the organic light-emitting diodes (OLEDs) instead of conventional LED, in which the brightness can be increased significantly. Feng et al. [6,7] developed an integrated micro-compressor element on the top surface of LGP and a micro-prism element at the bottom surface. By adjusting micro-prisms' shape, the LGP is able to control the illumination angle, and by adjusting micro-prisms' distribution and size, the LGP can achieve a uniform intensity. A series of experiments was performed by Han et al. [8] to investigate the effects of cavity conditions on transcription molding of micro-scale prisms made of PMMA. It was found that melt filling of V-grooves can be affected by the pitch, direction of grooves layout, direction of melt flow and cavity pressure. It was concluded that the transcription during the melt filling stage dominates the entire transcription process. Typically, an ideal layout of V-grooves can be optimized by an optical simulation [6,7]. However, a relation between molding conditions and resulting luminance performance has never been reported. In study [9], measurements of the depth of melt filling of V-groove structures in LGPs made of two different grades of PC as a function of molding conditions were carried out. The influence of molding processing conditions on degree of filling of V-grooves and luminance performance of LGPs was recently elucidated. In particular, the luminance of LGPs made of optical grade polycarbonates was measured and found to be affected by the depth of melt filling of the grooves. Recently, experimental and numerical investigations of the transcriptability during injection molding of microrib structures on plates were also reported using a generalized Newtonian fluid [10].

Over the years, a number of attempts on modeling the residual stresses and molecular orientation in injection molding of amorphous polymers have been made by various researchers. A brief review on the subject matter was given in Part I of this study [11]. Part I also described a numerical simulation of one- and two-dimensional flow using a control volume/finite element/finite difference method (CV/FEM/FDM) in injection molding process of an optical products. Numerical results were given on CD substrate including the filling, packing and cooling stages [11]. The compressible Leonov model [12] is used to calculate the flow stresses and the flow birefringence related to the flow stresses through an empirical linear stress-optical rule [13]. In carrying out the viscoelastic simulations, an unconditionally stable upwinding scheme [14] is used to remedy the limitations on small time step requirements of the previous calculations, as discussed in Ref. [11]. The linear viscoelasticity and photo-viscoelasticity together with the first order rate equation for the volume relaxation [15,16] are employed to calculate the thermal stresses and the thermal birefringence using a combination of constrained and free quenching approaches. The orientation functions, equation of state and elastic recovery are used to simulate the anisotropic shrinkages.

In the present study, extensive injection molding experiments are performed to manufacture LGP moldings of PS and two optical grades PCs at different processing conditions. The normal and two transverse components of birefringence in LGP moldings are measured. The importance of the thermally-induced birefringence is elucidated especially in LGP moldings of PCs. The numerical results for pressure field, thermally- and flow-induced birefringence and anisotropic shrinkages are obtained on global scale without inclusion of the local effects arising from filling microfeatures. The simulations are compared with experimental data on LGP moldings. In addition, a relevance of the frozen-in birefringence to the luminance of LGP molding is established.

## 2. Experimental

### 2.1. Materials and their properties

Two optical grade polycarbonates (PCs), PC OQ1030 (MFI of 12.8 g/10 min at 250 °C) and PC OQ3820 (MFI of 7.4 g/10 min at 300 °C), from GE Plastics are used to injection mold light-guide plate (LGP). In addition, LGPs from polystyrene (PS) Styron 615-APR from Dow Chemical Company are injection molded. The glass transition temperatures of these PCs measured by DSC (TA Instrument) at heating rate of 15 °C/min indicated the $T_g$ of 143.7 °C and 147.6 °C for PC OQ1030 and PC OQ3820, respectively. An ARES rheometer (TA Instrument) with parallel plates is used to measure the complex viscosity curves of PCs in a frequency range from 0.04 to 100 $s^{-1}$ and strain amplitude of 4% at various temperatures. The PC pellets were dried under vacuum at 105 °C for 4 h to remove moisture and compression molded at 250 °C and 260 °C for PC OQ1030 and PC OQ3820, respectively, into a disk of 2 mm in thickness and 2 cm in diameter. Fig. 1 shows the measured complex viscosity as a function of frequency for PCs at different melt temperatures. The Cox–Merz rule was used to obtain the steady-state shear viscosity as a function of the shear rate. The temperature shift factors are obtained for shear viscosity curves of PCs at a reference temperature, $T_r$, of 210 °C and fitted to the WLF equation:

$$\ln a_T = \frac{-C_1(T - T_r)}{C_2 + T - T_r} \tag{1}$$

where $C_1$ and $C_2$ are the WLF constants. The measured and fitted shift factors as a function of temperature for both PCs are shown in Fig. 2. The obtained WLF constants are then used to fit the viscosity data curves to the multimode Leonov viscosity model [12]:

$$\eta(\dot{\gamma}) = \eta_0 s + \sum_{k=1}^{N} \frac{\eta_k}{1 + X_k} \quad X_k = \sqrt{1 + 4\dot{\gamma}^2\theta_k^2} \tag{2}$$

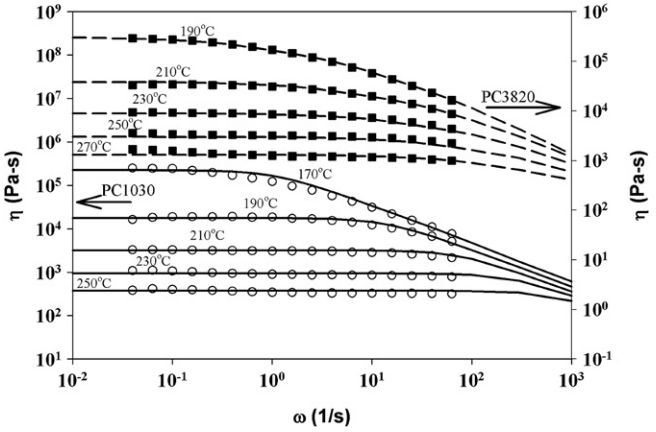


**Fig. 1.** Measured (symbols) and fitted (curves) viscosity of PC OQ1030 and PC OQ3820 at different temperatures.

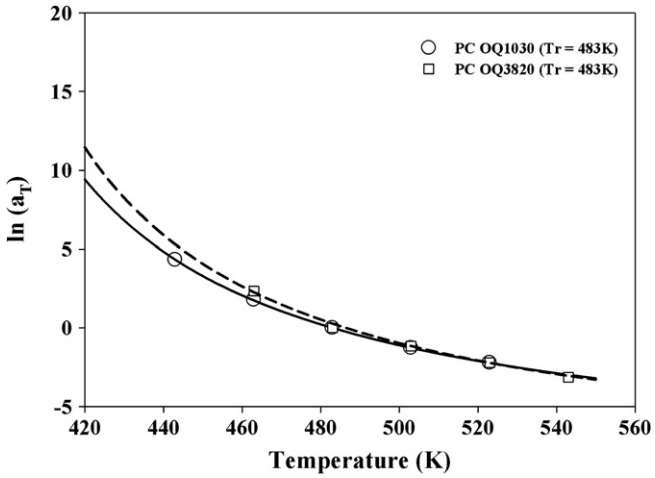


**Fig. 2.** Measured (symbols) and fitted (curves) temperature dependence of shift factors of PC OQ1030 and PC OQ3820 at a reference temperature of 210 °C.

where $\eta_k$ and $\theta_k$ are the $k$th mode shear viscosity and relaxation time, respectively, $N$ is the number of relaxation mode, $s$ is the factor between 0 and 1. Eq. (2) was fitted simultaneously by using the nonlinear least square method [17]. Two and four relaxation modes were employed for PC OQ1030 and PC OQ3820, respectively. The use of two relaxation modes for PC OQ1030 was due to the fact that at the same melt temperatures the non-Newtonian behavior in this melt occurs at much higher shear rates than in the PC OQ3820 melt. Fig. 1 shows measured (symbols) and fitted (curves) shear viscosity of PC OQ1030 and PC OQ3820 as a function of shear rate at different temperatures. Typical shear thinning behavior was observed for both PCs. It is seen that PC OQ3820 due its higher molecular weight exhibits nearly one order magnitude higher viscosity than that of PC OQ1030 at all temperatures.

Viscosity data, shift factors and rheological parameters for PS with two relaxation modes were earlier reported in Part I [11]. All rheological parameters and physical properties used in the injection molding simulation are shown in Table 1. The specific volume data for the optical grade PCs were taken from the MOLDFLOW database [18] described by the Tait equation.

### 2.2. Injection molding of LGP

The PC pellets were dried under vacuum at 105 °C for 4 h before molding. LGP moldings are obtained by using a Van Dorn 55F screw injection molding machine at various processing conditions. A schematic representation of the LGP mold is shown in Fig. 3. It includes two LGP cavities with a width of W = 47.45 mm and a length of L = 35.15 mm. A pressure transducer, KISTLER 6171BA, was installed at the nozzle of the injection molding machine. The thickness of LGP cavity, 2b, was varied along the width direction as shown in Fig. 3a. The thickness variation was made in order to provide a concentration of light. The V-groove patterns were made on the concave side of the LGP mold [9]. The injection molding experiments were performed under different processing conditions by varying injection speed, packing pressure, packing time, mold temperature and melt temperature. The processing conditions used are given in Table 2 for two PCs and in Table 3 for PS. A constant cooling time of 20 s was applied at all conditions.

### 2.3. Birefringence and anisotropic shrinkage in LGPs

To measure the birefringence distribution of LGP moldings, a polarized optical microscope of Leitz Laborlux 12POL S is used. It is equipped with a 4th and 30th order compensator (Leitz Laborlux) to measure the optical retardation. The specimens are prepared by cutting a slice of about 500 μm in thickness from the LGP moldings at the positions under investigation by using a diamond saw (Buehler Isomet) equipped with an oil bath. The specimens are cut in the direction parallel and perpendicular to the flow direction. A constant cutting speed of 60 rpm is used during cutting. Two transverse optical retardations were obtained from these slices. The thickness of slices is measured by a Digimatic micrometer (Mitutoyo). Once the optical retardations are obtained, the birefringence is determined as $\Delta n = \Gamma/c$, where $\Gamma$ is the measured optical retardation and $c$ is the thickness of slices. Also, the normal retardation is measured directly by the polarized optical microscope without cutting the LGP moldings. A schematic representation of three measured birefringence components is shown in Fig. 4.

The dimensions of LGP moldings in the length and width directions are measured by a Digimatic caliper (Mitutoyo) and in the thickness direction by a Digimatic micrometer (Mitutoyo). To calculate the percent shrinkages, the difference between part and mold dimensions is divided by the mold dimensions. The thickness profile of the mold indicated in Fig. 3a is determined by the MicroProf optical profiler (FRT of America). The thickness shrinkage is measured at the portion of the highest thickness. It should be noted that the error of measurements of various shrinkages is less than 2%.

**Table 1**
Material specification and parameters for PCs and PS.

| | PC-Q1030 | PC-OQ3820 | PS Styron 615 |
|---|---|---|---|
| *WLF Equation* | | | |
| $C_1$ | 9.11 | 8.42 | 8.28 |
| $C_2$ (K) | 124.0 | 138.6 | 131.9 |
| $T_r$ (K) | 483.0 | 503.0 | 473.5 |
| *Leonov model* | | | |
| Ref. [19] for PS | | | |
| $s$ | 0.0005 | 0.0001 | 0.00484 |
| $T_r$ (K) | 483.0 | 503.0 | 473.5 |
| $\eta_1$ (Pa s) | 3113.0 | 1306.7 | 2228 |
| $\theta_1$ (s) | 0.00972 | 0.72897 | 0.1466 |
| $\eta_2$ (Pa s) | 59.27 | 4326.8 | 446.8 |
| $\theta_2$ (s) | 0.0003267 | 0.062523 | 0.00489 |
| $\eta_3$ (Pa s) | | 2885.8 | |
| $\theta_3$ (s) | | 0.0053626 | |
| $\eta_4$ (Pa s) | | 341.99 | |
| $\theta_4$ (s) | | 0.00045995 | |
| Tait equation for PC [18] and PS [19] | | | |
| $b_{1l}$ ($m^3$/Kg) | 8.647e-4 | 8.647e-4 | 9.799e-4 |
| $b_{1s}$ ($m^3$/Kg) | 8.647e-4 | 8.647e-4 | 9.799e-4 |
| $b_{2l}$ ($m^3$/Kg-K) | 5.712e-7 | 5.712e-7 | 5.788e-7 |
| $b_{2s}$($m^3$/Kg-K) | 2.157e-7 | 2.157e-7 | 2.429e-7 |
| $b_{3l}$ (N/$m^2$) | 1.739e8 | 1.739e8 | 4.615e8 |
| $b_{3s}$ (N/$m^2$) | 2.564e8 | 2.564e8 | 3.301e8 |
| $b_{4l}$ ($K^{-1}$) | 4.390e-3 | 4.390e-3 | 3.019e-3 |
| $b_{4s}$ ($K^{-1}$) | 2.989e-3 | 2.989e-3 | 1.380e-3 |
| $b_5$ (K) | 416.0 | 416.0 | 376.0 |
| $b_6$ (K/Pa) | 3.77e-7 | 3.77e-7 | 3.20e-7 |
| $\Delta n^0$ [20] | 0.236 | 0.236 | −0.195 |
| $C_\sigma$ ($Pa^{-1}$) | 6.0E-11 [21] | 9.0E-ll [21] | −5.2E-9 [21] |
| $k$ (J/m s K) [22] | 0.260 | 0.260 | 0.122 |
| $C_p$ (J/Kg K) [22] | 2080 | 2080 | 2050 |

## 3. Comparison with experiment

### 3.1. Finite element mesh

The numerical simulations of injection molding process of LGP are carried out by the CV/FEM/FDM scheme using a Compaq Visual

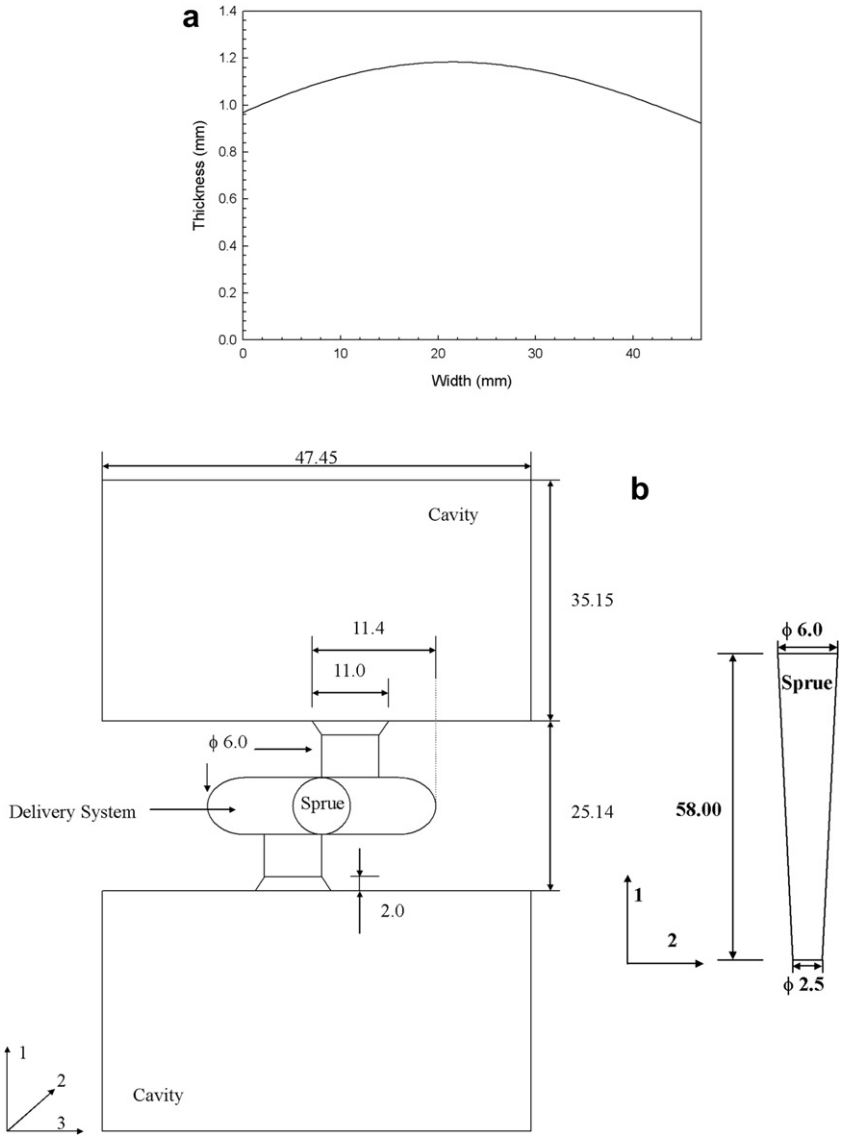


**Fig. 3.** Mold used in LGP molding experiments. (a) A cavity thickness variation; (b) a planar view and sprue. Gate thickness is 0.82 mm.

FORTRAN Version 6.2 of scientific language compiler. Details of numerical algorithm are reported in Part I [11]. A personal computer equipped with a single core Pentium IV 2.8 GHz CPU and 1 GB of physical memory is used to perform all calculations in a Windows XP platform. The mesh is generated over the mold cavity and the delivery system. The two-dimensional triangular finite elements are created over the plane of the mold cavity and fan gate. The one-dimensional tubular elements are used over the entire delivery system including the nozzle, sprue and runners. The total number of elements including one- and two-dimensional elements was 676. The total number of nodes was 381. These are shown in Fig. 5. The thickness direction was discretized by 40 nodes

**Table 2**
Processing conditions for injection molding of LGPs of PC OQ1030 and PC OQ3820.

| Run # | Injection Speed (cm/s) | Packing pressure (MPa) | Packing time (s) | Mold temperature (°C) | PC1030 melt temperature (°C) | PC3820 melt temperature (°C) |
|---|---|---|---|---|---|---|
| 1 | 2.54 | 34.47 | 5 | 100 | 270 | 280 |
| 2 | 5.08 | 34.47 | 5 | 100 | 270 | 280 |
| 3 | 7.62 | 34.47 | 5 | 100 | 270 | 280 |
| 4 | 2.54 | 20.68 | 5 | 100 | 270 | 280 |
| 5 | 2.54 | 55.16 | 5 | 100 | 270 | 280 |
| 6 | 2.54 | 34.47 | 2 | 100 | 270 | 280 |
| 7 | 2.54 | 34.47 | 10 | 100 | 270 | 280 |
| 8 | 2.54 | 34.47 | 5 | 80 | 270 | 280 |
| 9 | 2.54 | 34.47 | 5 | 100 | 260 | 290 |
| 10 | 2.54 | 34.47 | 5 | 100 | 280 | 300 |
| 11 | 2.54 | 34.47 | 5 | 110 | 270 | 280 |

**Table 3**
Processing conditions for injection molding of LGPs of PS Styron 615.

| Run # | Injection speed (cm/s) | Packing pressure (MPa) | Packing time (s) | Mold temperature (°C) | Melt temperature (°C) |
|---|---|---|---|---|---|
| 1 | 2.54 | 34.47 | 5 | 50 | 235 |
| 2 | 2.54 | 34.47 | 2 | 50 | 235 |
| 3 | 2.54 | 34.47 | 5 | 50 | 255 |

equally spaced throughout the cavity and delivery system for the finite difference calculation. The mesh density was refined during trial computations until simulated results were converged.

### 3.2. Melt front propagation

To observe the melt front propagation, a series of short shot experiments are carried out. The observed melt front propagations are compared with those predicted by simulation. Fig. 6 shows the measured (symbols) and calculated (curves) melt front propagation during the filling of the LGP cavity. The results show that the measured and calculated melt fronts are in fair agreement. A discrepancy between the simulation and experimental data near the side walls is apparently due to the presence of the inertial effect during the melt front propagation of the low viscosity PC OQ1030. The inertial effect was neglected in the present simulation. A more discussion concerning this effect will be given in the next section. A waviness of the calculated melt front is due to the fact that lines are directly obtained at the melt front nodes. These nodes are determined by the fill factors of the control volume, as described in [11]. To obtain a smooth melt front, a further refinement of finite element mesh is required. However, this could lead to a significant increase of the calculation time. Also, it may cause the convergence problem in the viscoelastic simulation [23].

### 3.3. Pressure evolution

Fig. 7 shows the measured and simulated pressure traces and screw position in Runs 1, 2 and 3 corresponding to different injection speeds for PC OQ1030 (a) and PC OQ3820 (b). Results are shown for the filling stage and initial portion of the packing stage. Changes of the pressure with time show a quite complex behavior

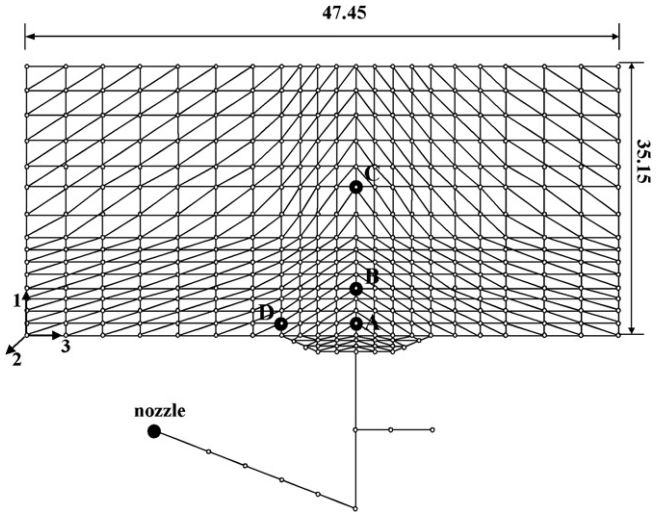


**Fig. 5.** Finite element mesh: two-dimensional triangular elements in the plane of the mold cavity and fan gate, and one-dimensional tubular elements in the delivery system used in simulations. Unit: (mm). The letters A, B and C indicate the locations where the transverse birefringence was measured. The letter D indicates the location where the thickness shrinkage was measured.

due to the shape of delivery system that includes nozzle, sprue, runners and gates. Also, the pressure variation within various stages is clearly seen. These include the filling stage, where variation of pressure with time shows several distinct regions of growth depending on the location of the melt front during the filling stage. In the filling stage, the pressure increases from zero to the maximum pressure at which time the cavity is filled. The shot size or volume of melt injected is determined by the difference between the maximum and minimum on screw position curves. The pressure development during the filling of runner system is completed at the time corresponding to a slow rise of the pressure (a pressure plateau is seen at a low injection speed). Then, the pressure starts to increases again due to the melt passing through the gate into the cavity. The pressure increases further until the end of the filling stage due to a significant increase of the resistance to flow such that a higher pressure is required to maintain a constant injection speed. After completion of the filling stage, the pressure quickly drops to the applied packing pressure. This pressure is maintained for the duration of the packing time needed to compensate for the melt

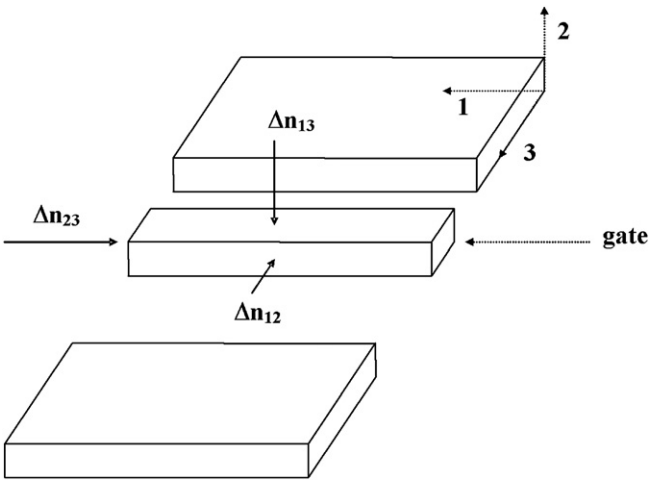


**Fig. 4.** Schematic representations of three birefringence components measured in LGP moldings. The arrows indicate the direction of polarized light. 1, 2 and 3 indicates the length, thickness and width direction, respectively.

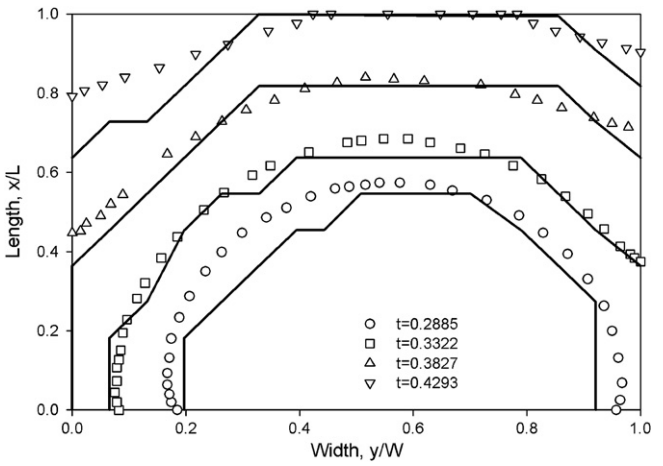


**Fig. 6.** Measured (symbols) and calculated (lines) melt front propagation in the LGP cavity in Run #1 for PC OQ1030.

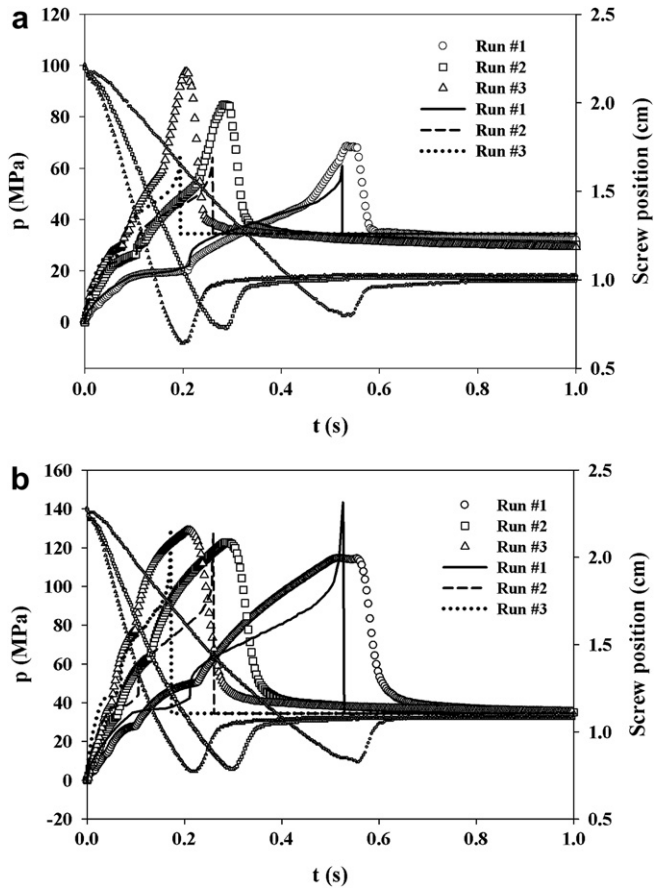


**Fig. 7.** Measured (symbols) and predicted (curves) pressure traces and measured screw positions (symbols) at different injection speeds during LGP molding of PC OQ1030 (a) and PC OQ3820 (b).

shrinkage due to cooling. In addition, it is important to note that the inertial effect of screw movement becomes more significant at higher injection speeds. This is indicated by the minimum of screw position curves in Fig. 7. It means that more melt is forced into the cavity with increasing injection speed, even though the shot size is set up to be a constant.

Clearly, the predicted pressure is in a fair agreement with experimental results of PC OQ1030 at low injection speed, but shows some deviations in PC OQ3820. This is due to the fact that constant injection speeds were difficult to maintain. The latter is indicated by a nonlinearity of the screw position vs. time curves, as seen in Fig. 7b for PC OQ3820. The variation of injection speed with time was less significant for the low viscosity PC OQ1030, but was more significant for the higher viscosity PC OQ3820. Also, it should be noted that in the filling stage a maximum injection pressure was imposed till the cavity was completely filled. Accordingly, the transfer of the pressure from the injection stage to the packing stage cannot be accomplished instantaneously. Therefore, the peak of the measured pressure does not coincide with the calculated pressure.

From Fig. 7a it is seen that the simulated pressure traces are in good agreement with experimental data until time corresponding to the completion of filling of runners at all the injection speeds. At the same time, for a low injection speed (Run #1), a good agreement between the measured and simulated pressure traces is obtained over the filling time. However, with increasing injection speed, a deviation is observed especially when the pressure increases due to the melt passing through the gate and into the cavity. It is seen from Fig. 7b, that in case of the PC OQ3820, a more deviation is observed in the filling stage. This is due to the fact that constant injection speed is no longer maintained. The variation of injection speed was less significant for the low viscosity PC OQ1030.

The maximum of the simulated pressures does not indicate a significant variation with the injection speed but the measured pressure does. This is due to the fact that the inertial effect of screw movement becomes considerable with an increase of the injection speed, as indicated by screw position curves in Fig. 7. It means that more material is forced into the cavity with increasing injection speed, even though the shot size is set up to be a constant. It is seen from Fig. 7, that at high injection speeds the inertial effect is more considerable in the low viscosity PC OQ1030 than that in the high viscosity PC OQ3820. The latter explains why the measured maximum pressure of PC OQ1030 increases significantly with increasing injection speed.

Fig. 8 exhibits a comparison of the measured and simulated pressure in Runs 1, 4 and 5 corresponding to different packing pressures in the filling stage and initial portion of the packing stage for PC OQ1030 (a) and PC OQ3820 (b), respectively. Pressures in the packing stage are defined by the packing pressure setups on the injection molding machine. Fig. 8 indicates that the pressure development is similar in the filling stage but different in the packing stage. A good agreement between the measured and

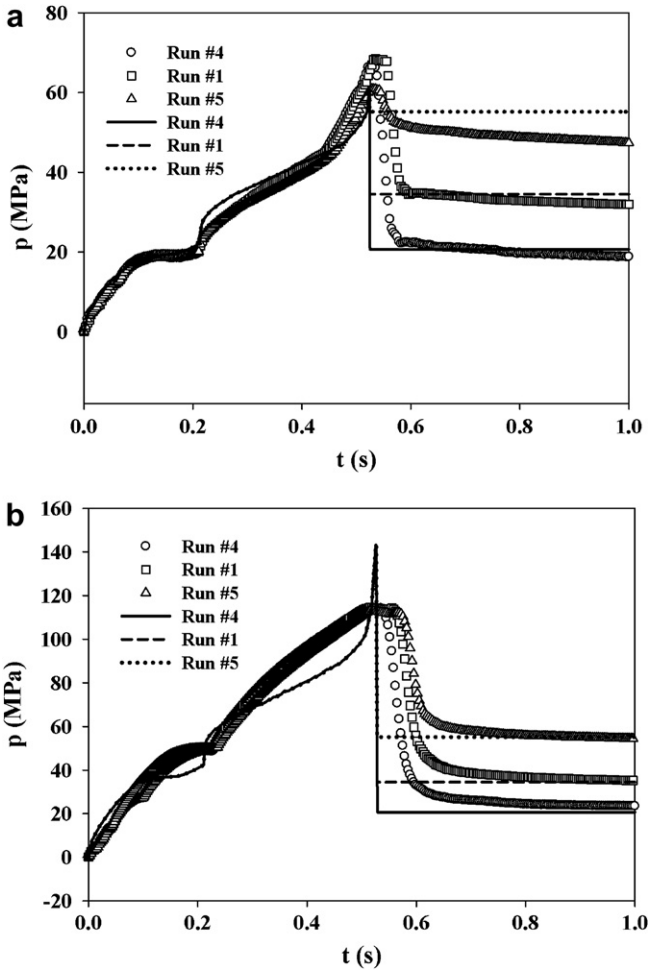


**Fig. 8.** Measured (symbols) and predicted (curves) pressure traces at the nozzle of the LGP mold at different packing pressures for PC OQ1030 (a) and PC OQ3820 (b).

predicted pressures is observed for PC OQ1030, but a deviation was observed for PC OQ3820 in the filling stage.

### 3.4. Birefringence development

#### 3.4.1. Transverse flow birefringence components

Birefringence developed in LGP moldings is very complex due to a two-dimensional flow in the LGP cavity. The transverse birefringence components, $\Delta n_{12}$ and $\Delta n_{23}$, are defined as the gapwise distribution of birefringence measured at 1–2 and 2–3 planes, respectively, as indicated in Fig. 4. Since the temperature difference between two neighboring material points along the gapwise direction during molding is significant, the contribution of the thermally-induced birefringence to the birefringence $\Delta n_{12}$ and $\Delta n_{23}$ is expected to be substantial. The nonlinear constitutive equation [12] used to describe flow behavior is not suitable to describe the development of the thermal stresses. Accordingly, the following discussions will only focus on the flow-induced transverse birefringence components. The contribution of the thermally-induced birefringence into the transverse birefringence components will be considered later.

The calculation of the elastic strain tensor is carried out in the streamwise (streamline) direction, which varies with the directions of the velocity and pressure gradient vectors [11]. Therefore, the calculated transverse birefringence components $\Delta n_{12s}$ and $\Delta n_{23s}$ in the streamwise coordinates have to be transferred into the Cartesian coordinate. The birefringence components $\Delta n_{12}$ and $\Delta n_{23}$ along the Cartesian coordinate were calculated as

$$\Delta n_{12} = \Delta n_{12,s}\frac{|\nabla p_1|}{\nabla p_s} + \Delta n_{23,s}\frac{|\nabla p_3|}{\nabla p_s} \tag{3}$$

$$\Delta n_{23} = \Delta n_{23,s}\frac{|\nabla p_1|}{\nabla p_s} + \Delta n_{12,s}\frac{|\nabla p_3|}{\nabla p_s} \tag{4}$$

$$\nabla p_s = \sqrt{\nabla p_1^2 + \nabla p_3^2} \tag{5}$$

where subscript $s$ represents the streamwise direction and $\nabla p_s$, $\nabla p_1$ and $\nabla p_3$ are the pressure gradients along the streamline ($s$), length ($x$) and width ($z$) directions, respectively. The values were calculated until the time when freezing occurs at the locations under consideration, since the pressure gradients are not available after this time.

Fig. 9 shows the gapwise distribution of the calculated flow birefringence components $\Delta n_{12}$ (a) and $\Delta n_{23}$ (b) at processing condition of Run #1 at locations A, B, and C of LGP moldings (see Fig. 5) of PC OQ1030 at the end of filling and cooling stages. Birefringence distribution shows patterns similar to those of PC disks [19]. At the end of the filling stage, a maximum value of $\Delta n_{12}$ happens near the wall due to the formation of the solidified layer. The thickness of this layer increases from location A, being close to the gate, to location C, being further away from the gate. In the packing stage, more melt is forced into the cavity to compensate for the shrinkage. This introduces a second maximum that is located further away from the wall. At the same time, the birefringence maximum near the wall relaxes causing a concave area between two maxima. It is also noted that the development of the second maximum is less significant at locations away from the gate (location C) due to a weak flow during the packing stage at this location. The gapwise distribution of the birefringence component $\Delta n_{23}$ is similar to that of $\Delta n_{12}$, but its value is negative and almost one order magnitude lower. Although the flow in the LGP cavity is two-dimensional, the locations under investigation have stronger flow in the direction of 1 than the direction of 3. Therefore, a higher

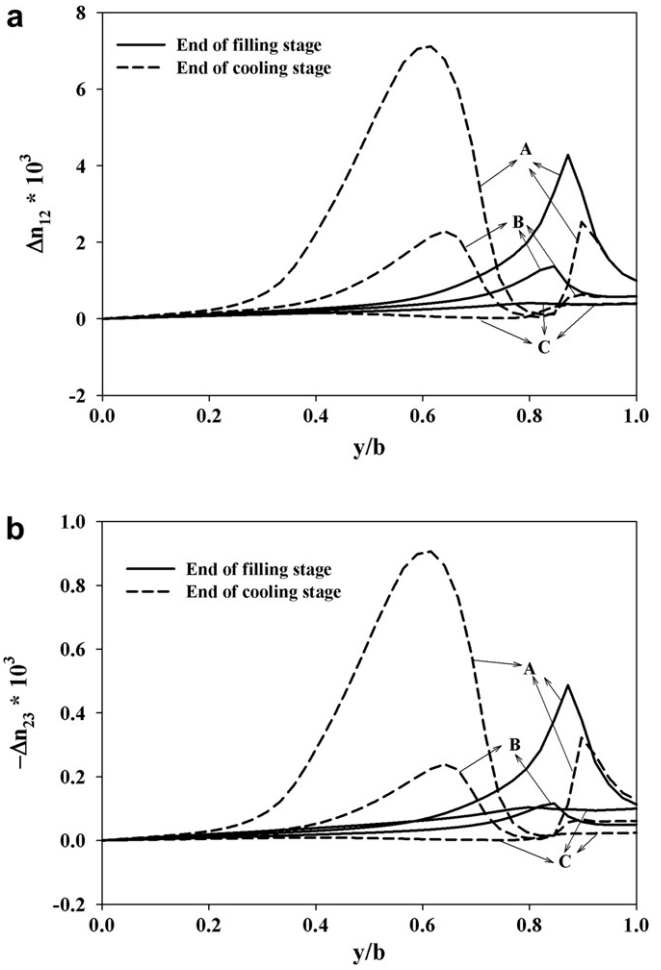


**Fig. 9.** Calculated birefringence components $\Delta n_{12}$ (a) and $\Delta n_{23}$ (b) at processing condition of Run #1 at locations A, B, and C in LGP moldings for PC OQ1030 at the end of filling and cooling stages.

pressure gradient acts along the direction of 1 resulting in higher value of $\Delta n_{12}$.

Fig. 10 shows a comparison of the gapwise distribution of the measured and calculated residual birefringence components $\Delta n_{12}$ (a) and $\Delta n_{23}$ (b) in the LGP molding of PC OQ1030 obtained in Run #1 at positions B and C. It indicates much higher values of the measured birefringence components $\Delta n_{12}$ and $\Delta n_{23}$ compared to those of simulations. This is due to the fact that the thermally-induced birefringence has a significant contribution to the overall birefringence which is not considered at this point. It is also seen that the measured values of birefringence components $\Delta n_{12}$ and $\Delta n_{23}$ at locations B and C are comparable indicating that the contribution from the thermally-induced birefringence to the residual birefringence components in LGP moldings is very important in addition to the flow-induced birefringence.

To understand the effect of processing conditions on the flow-induced birefringence, Figs. 11 and 12 display the predicted residual flow birefringence $\Delta n_{12}$ in LGP moldings obtained at different injection speeds (a), packing pressures (b), packing times (c), mold temperatures (d) and melt temperatures (e) for LGP moldings of PC OQ1030 and PC OQ3820, respectively. Figs. 11a and 12a show the predicted value of $\Delta n_{12}$ at locations B and C in LGP moldings obtained at different injection speeds for PC OQ1030 and PC OQ3820, respectively. Both PCs exhibit distinct patterns in the development of $\Delta n_{12}$. In particular, the LGP of PC OQ1030 indicates a highly

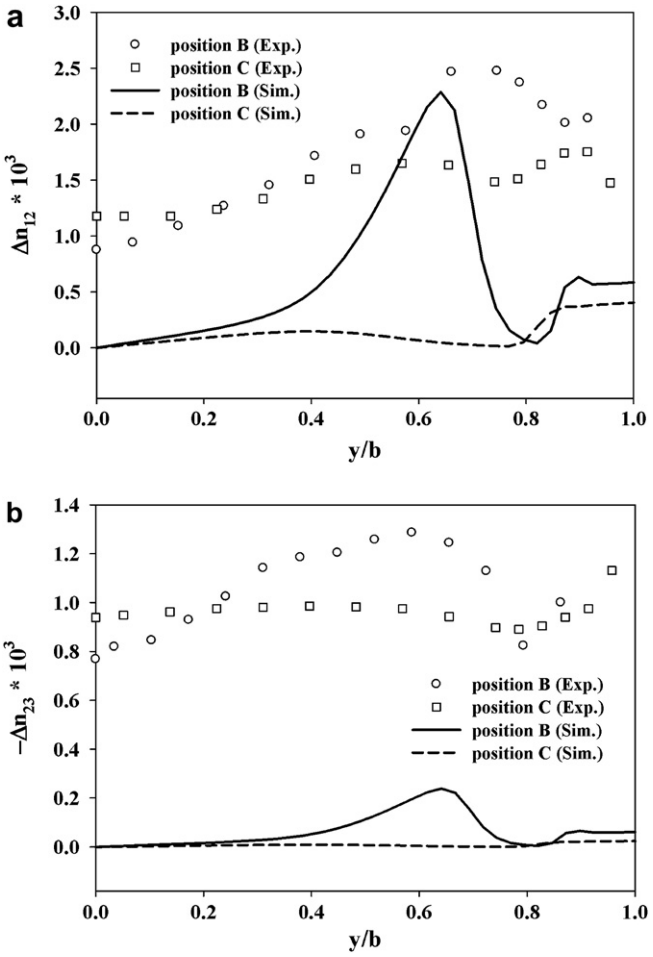


**Fig. 10.** Measured (symbols) and calculated (curves) gapwise birefringence components $\Delta n_{12}$ (a) and $\Delta n_{23}$ (b) at processing condition of Run #1 at locations B and C in LGP moldings of PC OQ1030.

pronounced maximum of $\Delta n_{12}$ further away from the wall, introduced due to the flow-induced birefringence in the packing stage, than that found in LGP of PC OQ3820. However, LGP moldings of PC OQ3820 develop a significantly higher maximum of the residual flow-induced birefringence near the wall (Fig. 12a) than LGP moldings of PC OQ1030 (Fig. 11a). The presence of the higher birefringence maximum near the wall is due to a nearly one order magnitude higher viscosity and relaxation time of PC OQ3820 leading to substantial retardation of the relaxation process of the transverse birefringence during cooling. Conversely, a lower level of the birefringence maximum near the wall in case LGP molding of PC OQ1030 is due to a faster relaxation process in this polymer. In addition, the LGP molding of PC OQ3820 shows a higher level of the flow-induced birefringence. This is due to the fact that PC OQ3820 has a higher stress-optical coefficient in the melt state [21]. Also, in LGP molding of PC OQ3820 higher shear and normal stresses are developed during cavity filling due to its high viscosity. Furthermore, an increase of the injection speed causes a lower maximum of $\Delta n_{12}$ further away from the wall and a lower birefringence near the wall, as indicated in Figs. 11a and 12a, but the effect is observed to be minor in LGP molding of PC OQ1030. This is due to shorter filling time and more viscous heating resulting in higher melt temperature in the cavity leading to a faster birefringence relaxation.

Figs. 11b and 12b show the gapwise distribution of the predicted birefringence component $\Delta n_{12}$ at locations B and C in LGP moldings obtained at different packing pressures for PC OQ1030 and PC OQ3820, respectively. It clearly indicates that the magnitude of the maximum of $\Delta n_{12}$ further away from the wall is significantly increased with the packing pressure. At the same time, the value of $\Delta n_{12}$ near the wall shows minor variation with the packing pressure. This effect is due to the fact that stresses near the wall are mostly frozen during the cavity filling stage.

Figs. 11c and 12c show the gapwise distribution of the predicted birefringence component $\Delta n_{12}$ at locations B and C in LGP moldings obtained at different packing times for PC OQ1030 and PC OQ3820, respectively. The predictions show a minor effect of the packing time on the birefringence. This is due to the fact, as shown by simulations, that gate freezes at time of 2.16 and 2.54 s for PC OQ1030 and PC OQ3820, respectively, at processing condition of Run #1. This gate freezing time is close to the shortest packing time applied in this study. Therefore, the predicted transverse birefringence component $\Delta n_{12}$ is only slightly affected by the packing time.

Figs. 11d and 12d show the gapwise distribution of the predicted birefringence component $\Delta n_{12}$ at locations B and C in LGP moldings obtained at different mold temperatures for PC OQ1030 and PC OQ3820, respectively. For PC OQ1030, as shown in Fig. 11d, the higher mold temperature significantly affects the birefringence maximum further away from the wall. This increase of the birefringence maximum is due to the fact that the higher mold temperature leads to a less resistance in the core melt flow allowing more melt to be pushed into the cavity. However, in case of LGP molding of PC OQ3820, as shown in Fig. 12d, the effect of the mold temperature on the birefringence maximum further away from the wall is less significant due to its high viscosity. At the same time, the birefringence near the wall decreases with an increase of the mold temperature. In addition, the maximum located further away from the wall in LGP moldings of both PCs is observed to be shifted towards the wall with increasing mold temperature. This is due to a lower cooling rate at a higher mold temperature resulting in a thinner solidified layer. This is also evident from the birefringence maximum located near the wall region that is also shifted closer to the wall with an increase of the mold temperature. In particular, a higher mold temperature allows a relatively faster relaxation near the wall region leading to a decrease of the birefringence in the wall region. This effect is more significantly pronounced in LGP moldings of PC OQ3820 than that of PC OQ1030.

Figs. 11e and 12e demonstrate the gapwise distribution of the predicted birefringence component $\Delta n_{12}$ at locations B and C in LGP moldings obtained at different melt temperatures for PC OQ1030 and PC OQ3820, respectively. It is seen that at location B of PC OQ1030 the value of the birefringence maximum further away from the wall significantly increases with reducing melt temperature, but an opposite tendency was observed at location C. This is due to a competition between buildup and relaxation of birefringence further away from the wall. Although a higher melt temperature accelerates the relaxation process, it also allows more melt to be pushed into the cavity due to its lower viscosity. In fact, LGP molding of PC OQ3820 shows that a buildup of the birefringence maximum further away from the wall is dominated by the relaxation process at location B. Therefore, the value of maximum $\Delta n_{12}$ further away from the wall increases with increasing melt temperature. The same tendency was observed at location C, but to a lesser extent.

As shown in Fig. 11e, the birefringence maximum $\Delta n_{12}$ in the wall region increases with reducing melt temperature. This is due to the fact that solidification of polymer at a lower melt temperature occurs at earlier time than that at a higher melt temperature. This effect is more pronounced at locations B and C of the LGP molding of PC OQ1030 than that of PC OQ3820. In fact, the birefringence maximum $\Delta n_{12}$ in the wall region of LGP molding of PC

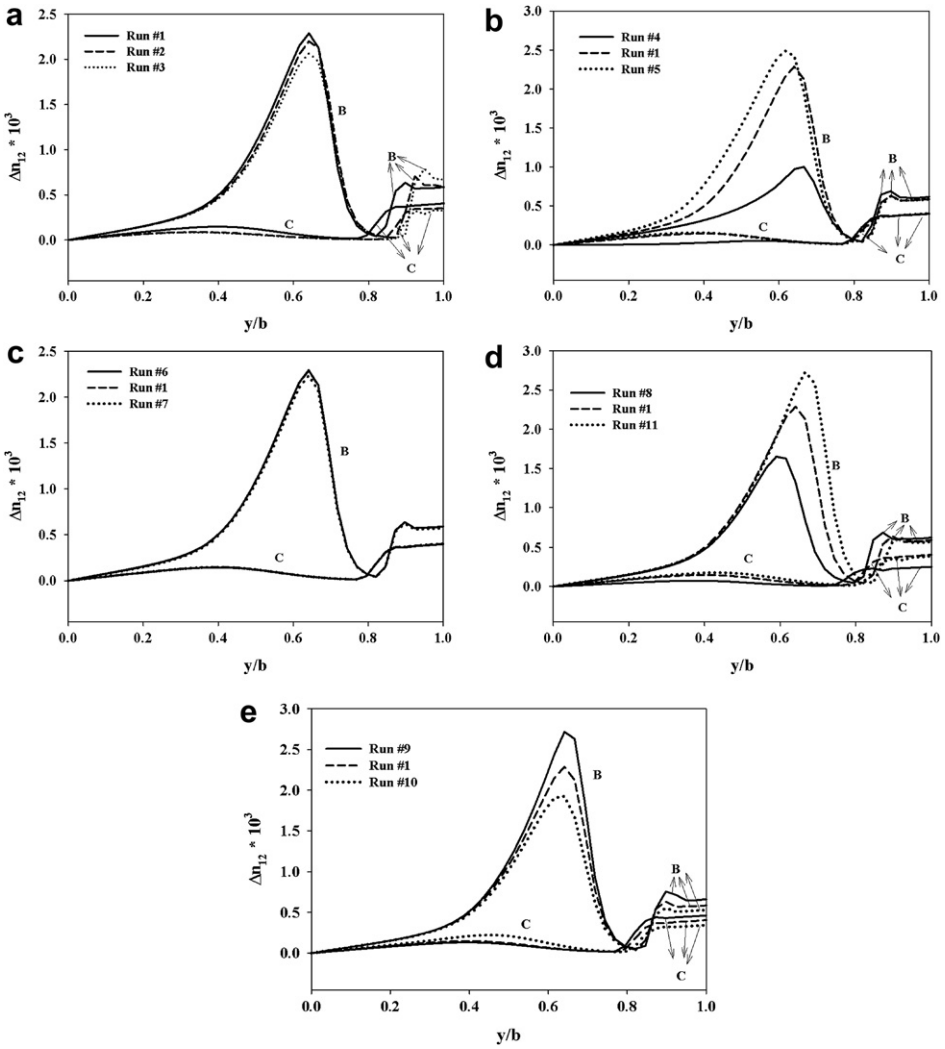


**Fig. 11.** Predicted gapwise distribution of birefringence $\Delta n_{12}$ at locations B and C for different injection speeds (a), packing pressures (b), packing times (c), melt temperatures (d) and mold temperature (e) in LGP moldings of PC OQ1030.

OQ3820 exhibits about similar value at various melt temperatures. This is due to the fact that in the high viscosity PC OQ3820 a slower relaxation of the birefringence occurs.

Fig. 13 demonstrates a comparison of the gapwise distribution of the predicted birefringence component $\Delta n_{12}$ at locations B and C in LGP moldings of PS 615 obtained in Runs #1 and #2, corresponding to different packing times, and in Run #1 and Run #3, corresponding to different melt temperatures (see Table 3). The value of the gapwise birefringence $\Delta n_{12}$ is all negative due to the negative stress-optical coefficient of PS 615 in the melt state [21]. The maximum birefringence further away from the wall at locations B and C increases with an increase of the packing time. This is due to the fact that more melt is pushed to the cavity to compensate for the shrinkage before the gate freezing. Unlike to LGP moldings of two PCs, in LGP molding of PS the packing time shows significant effect on the development of the birefringence maximum further away from the wall. This is because the calculated gate freezing time in LGP molding of PS in Run #1 is 3.35 s in contrast to 2.16 s and 2.54 s in Run #1 for PC OQ1030 and PC OQ3820, respectively. In addition, the birefringence maximum in the wall region shows a little effect with a change of the packing time. This is due to the fact that the development of the birefringence in this region was mainly completed in the filling stage. Also, Fig. 13 shows that the birefringence maximum further away from the wall at locations B and C in LGP moldings increases with an increase of the melt temperature. This is due to the fact that at the higher melt temperature more melt can be pushed into the cavity due to its lower viscosity, thus overriding the effect of the relaxation process. In particular, the birefringence maximum in the wall region at locations B and C indicates a decrease with an increase of the melt temperature. This is because a lower level of the flow stresses induced at a higher melt temperature.

### 3.4.2. *Thermally-induced birefringence*

The thermally-induced birefringence is caused by the nonequilibrium density and the viscoelastic behavior of polymers during an inhomogeneous rapid cooling through the glass transition temperature. The nonlinear constitutive equation used to describe the flow birefringence is not suitable to describe the development of the thermal stresses and birefringence during cooling from the rubbery to glassy state. During cooling polymeric materials exhibit a small deformation, therefore linear viscoelastic and photoviscoelastic constitutive equations are suitable to evaluate the evolution of the thermally-induced birefringence. The mathematical modeling and algorithm for simulations of the thermally-induced stresses and birefringence was described in Part I [11]. To carry out simulations of the thermal birefringence in LGP moldings the master curves of the

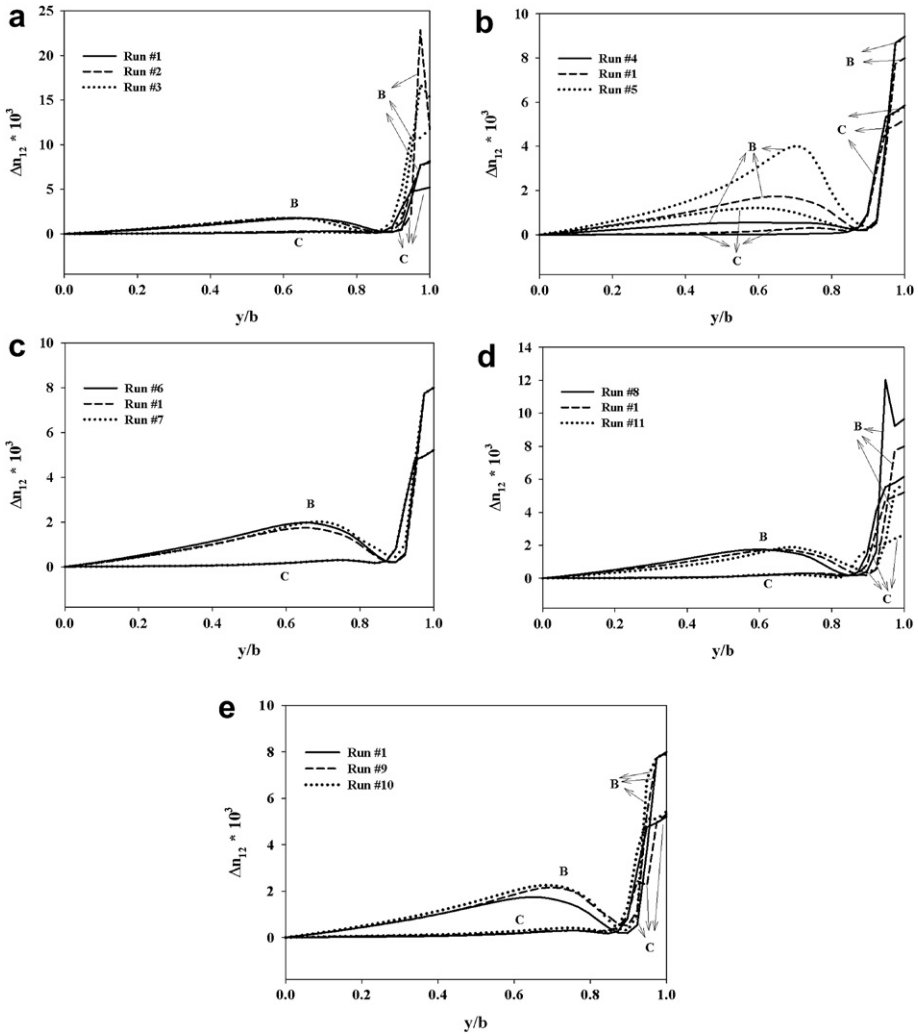


**Fig. 12.** Predicted gapwise distribution of birefringence $\Delta n_{12}$ at locations B and C for different injection speeds (a), packing pressures (b), packing times (c), melt temperatures (d) and mold temperatures (e) in LGP moldings of PC OQ3820.

relaxation modulus and strain optical coefficient functions along with the master curve of shift factors and physical properties of polymers are required. These data for both PCs and PS are taken from Refs. [21] and [16], respectively. It should be noted that the presence

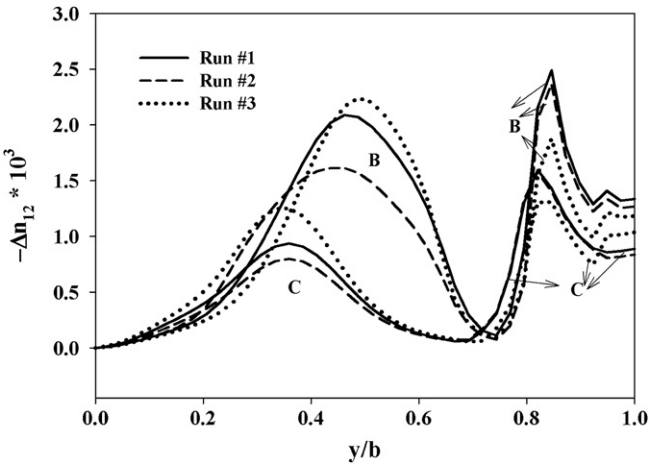


**Fig. 13.** The predicted gapwise distribution of birefringence $\Delta n_{12}$ at locations B and C at different processing conditions in LGP moldings of PS 615.

of the mold wall may dramatically affect the strain and birefringence development during cooling due constraints at the mold boundary. Due to adhesion of melt to the wall, the stresses will not equilibrate. The thermal expansion coefficient of polymer is considerably higher than that of the steel mold. Therefore, during cooling process only tensile stresses will buildup until the polymer is detached from the wall. After detachment, cooling would take place under free quenching boundary condition. The thermal expansion of the mold wall is considered to be sufficiently small such that its effect is negligible.

Fig. 14 shows the gapwise distribution of the transient thermally-induced birefringence calculated by a combination of the constrained and free quenching assumption at location B of LGP moldings of PC OQ1030 (a) and PS 615 (b). The first curve at time of 0.08 s for PC OQ1030 and 0.02 s for PS 615 indicates that there is a very fast buildup of the thermally-induced birefringence near the wall. This is caused by the instant freezing of melt at the mold wall. Then, the thermal birefringence growth propagates further towards the core until the calculated cavity pressure is non-zero. The thermal birefringence in the core is still negligible at this point, since the core melt is still hot. The constrained quenching algorithm is applied at this stage leading to the lateral strains caused by the action of the melt pressure [11]. The curve corresponding to 3.8 s in case of PS 615 indicates the time when

pressure drops to zero (Fig. 14b). At that instant the free quenching condition is applied and the thermal birefringence in the center region starts to develop due to the fact that the melt temperature is reduced to the value being close to $T_g$. In case of PC OQ1030, the pressure is still acting even at later time, 5 s (Fig. 14a). Therefore, the constrained cooling is still applied. The birefringence in the wall region does not relax since the tensile stress is developed due to constrained cooling. After pressure is reduced to zero, the calculation continues until cooling time of 30 s when equilibrium state is reached. The final thermally-induced birefringence indicates a parabolic shape in the core region as reported in the case of the free quenching condition [16,21]. A very similar birefringence distribution can be seen in the core region by comparing results obtained in the free quenching of PS (Fig. 14b). However, a higher birefringence in the core region was observed in case of combination of constrained and free quenching than in free quenching alone. This is due to the tensile stress developed during the constrained cooling. The thermal birefringence corresponding to the equilibrium indicates the occurrence of some relaxation in extended wall region, except at the wall. This effect at the wall is due to the imposed temperature boundary condition, $T = T_w$. In case of PS, the equilibrated thermal birefringence exhibits negative value over the thickness. In contrast, in case of free quenching, the negative birefringence in the core region and the positive birefringence in the wall region are observed [16]. The difference between these behaviors of the thermal birefringence in molding and free quenching is due to the development of the tensile stresses in the wall region in case of constrained quenching.

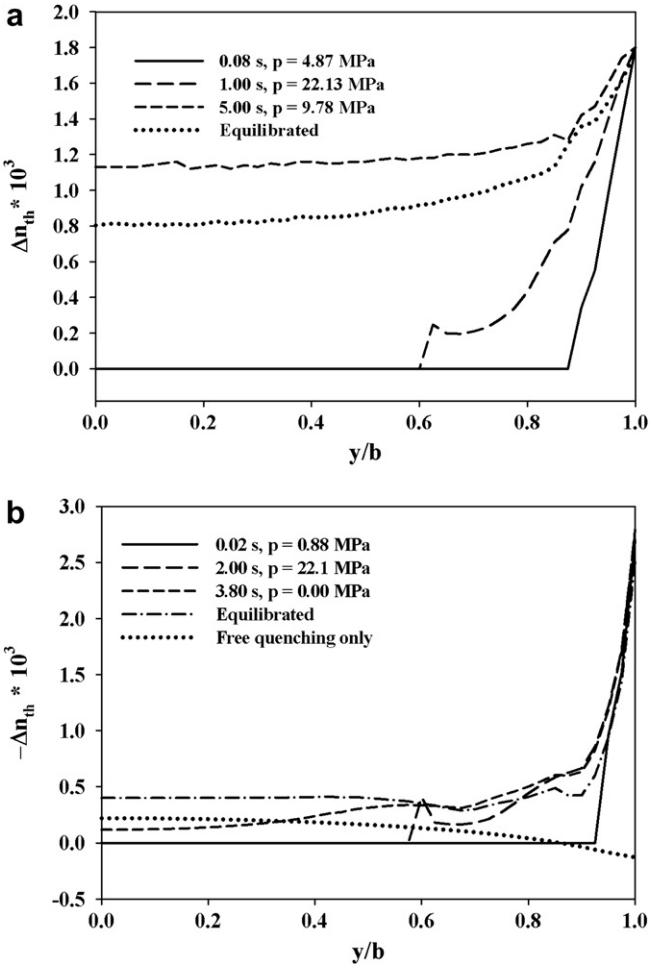


**Fig. 14.** Gapwise distribution of the transient thermally-induced birefringence calculated by a combination of the constrained and free quenching assumption at location B of LGP molding of PC OQ1030 (a) and PS 615 (b) in Run #1.

Fig. 15 displays a comparison of the gapwise distribution of the calculated residual thermally-induced birefringence at locations B and C in LGP moldings of PC OQ1030 (a), PC OQ3820 (b) and PS 615 (c) at processing conditions of Run #1. Interestingly, both PCs show a similar behavior of the thermal birefringence while PS shows a different behavior, as indicated in Fig. 16c. In case of PS, the thermal birefringence varies only slightly with locations. Such a tendency was observed in numerical study of the residual thermal stresses in molded slabs [24]. At position B of LGP moldings of both PCs the pressure is still non-zero even the temperature reduced to below $T_g$. At the same time, at position C of LGP moldings of both PCs, the thermal birefringence distribution, similar to free cooling, demonstrates a parabolic shape in the core region. However, birefringence increases towards the wall region with a maximum being at the wall due to constrained cooling. This parabolic shape of the thermal birefringence in the core region is due to an earlier release of the pressure at the location C, since it is further away from the gate. It means if the constraint is released as soon as the skin is solidified, the thermal birefringence distribution in the core region of LGP molding will be similar to that of the free quenching. Therefore, the duration of constrained cooling is clearly an important factor in defining the shape and magnitude of the thermally-induced birefringence. In addition, at the same location, LGP moldings of both PCs show about similar values of the thermal birefringence in the core regions and at the wall.

A comparison of the gapwise distribution of the calculated residual thermally-induced birefringence at locations B and C in LGP moldings of PS 615 obtained at different processing conditions for Runs #1 and #2, corresponding to different packing times, and for Run #1 and Run #3, corresponding to different melt temperatures, was made (data were not presented). It was found that among three processing conditions, the thermal birefringence was almost identical. A slightly lower birefringence is observed at processing condition of Run #2 corresponding to the lowest packing time of 2 s. This implies that at processing condition of Run #2, LGP molding experienced a shorter time at the constrained cooling than that of Runs #1 and #3. Therefore, the duration of the constrained cooling might be a dominating factor in the development of the thermally-induced birefringence. The thermal birefringence in the core region observed at processing condition of Run #2 is due to a shorter duration of the constrained cooling than that in LGP moldings of PCs. In case of PS, the thermal birefringence is significant in the wall region.

### 3.4.3. Total transverse residual birefringence

The calculated thermally- and flow-induced birefringence is added to obtain the calculated total residual birefringence in LGP moldings. Fig. 16 shows the gapwise distribution of the experimental and calculated total residual birefringence $\Delta n_{12}$ at locations B and C of LGP moldings of PC OQ1030 (a), PC OQ3820 (b) and PS 615 (c) and the experimental and calculated total residual birefringence $\Delta n_{23}$ at locations B and C of the LGP molding of PC OQ1030 (d) obtained in Run #1. The measured and predicted total birefringence at position B is slightly higher than that at location C, since location B is closer to the gate. Predictions are in a qualitative agreement with measurements with results at location C being generally in a better agreement. This is evidently due to a less influence of the flow through the gate on birefringence at location C, which is further away from the gate. Also, it is noted that in LGP moldings of PS the contribution of the thermal birefringence to the total birefringence is less significant except near the wall.

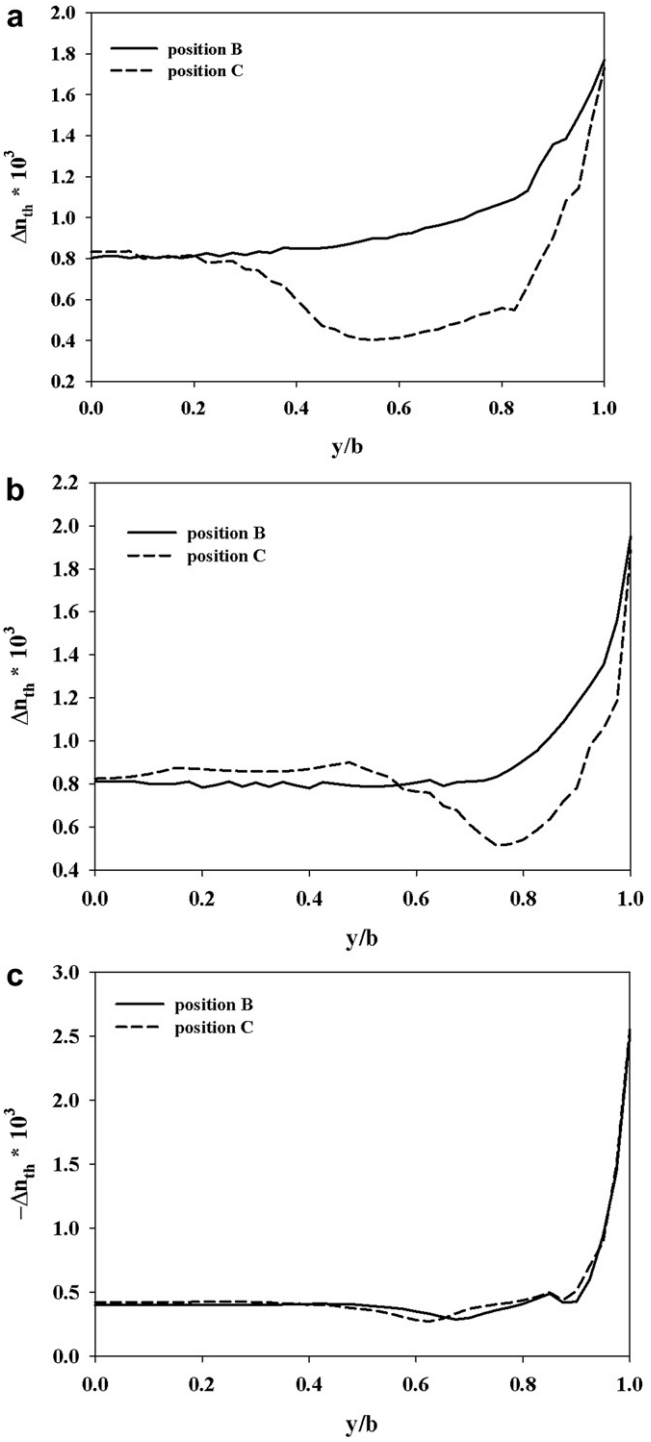


**Fig. 15.** Comparison of calculated residual thermally-induced birefringence in the gapwise direction at locations B and C in LGP moldings of PC OQ1030 (a), PC OQ3820 (b) and PS 615 in Run #1.

### 3.4.4. Normal residual birefringence

The normal birefringence is defined as the averaged normal component of birefringence that is measured in the 1–3 plane perpendicular to the gapwise direction. The thermally-induced birefringence is negligible in this plane since cooling mainly takes place along the gapwise direction. Then the thickness averaged normal birefringence, $<\Delta n_{13}>$, is used to obtain the normal birefringence:

$$\langle \Delta n_{13} \rangle = \frac{1}{b} \int_0^b \Delta n_{13}(z) dz \tag{6}$$

Fig. 17 shows the simulated and measured normal birefringence $\langle \Delta n_{13} \rangle$ along the flow direction (A–C direction in Fig. 5) at various injection speeds in Runs #1, 2 and 3 (a), packing pressures in Runs #4, 1 and 5 (b), packing times in Runs #6, 1 and 7 (c), mold temperatures in Runs #8, 1 and 11 (d) and melt temperatures in Runs #9, 1 and 10 (e) for PC OQ1030 and PC OQ3820. Comparisons of results indicate that LGP moldings of PC OQ3820 exhibit consistently higher normal birefringence than those of PC OQ1030. It is caused by a higher stress-optical coefficient in the melt state [21] and also higher normal and shear stresses resulting from higher viscosity and relaxation time of PC OQ3820, as indicated in Fig. 2 and Table 1. LGP moldings of both PCs show not only different level of the measured normal birefringence, but also different patterns. The measured normal birefringence along the flow direction demonstrates the highest value near the gate due to a high level of molecular orientation and decreases along the flow direction. However, the measured normal birefringence of PC OQ1030 exhibits a sudden increase then decreases near the gate forming a maximum. This maximum is typically not observed in PC OQ3820. However, such a maximum of the normal birefringence of PC OQ3820 was observed only in Run #10 corresponding to high melt temperature. It seems that a lower melt viscosity may be the cause for a maximum of the normal birefringence, since the development of birefringence close to the gate is a competition between the buildup and relaxation processes during melt flow near the gate area. Such a buildup and relaxation of birefringence generally occurs in contraction and expansion flows [25].

Fig. 17a shows the effect of injection speed on the measured normal birefringence with the lowest injection speed indicating somewhat higher value of birefringence in case of PC OQ3820. This is due to the lower shear rate and less viscous heating leading to a dominating effect of the relaxation process which is retarded at a low injection speed. In contrary, the measured normal birefringence of PC OQ1030 is not affected at all by the injection speed at distances more than 6 mm away from the gate. This is due to a freezing effect on formation of birefringence. Overall, the injection speed is not a significant processing parameter affecting the development of the normal birefringence in LGP. In fact, the simulated normal birefringence of PC OQ1030 does not show that it is affected by the injection speed at all. The simulation is able to predict the level of the residual normal birefringence, but unable to describe the exact shape of curves, especially the formation of the maximum. This may be due to the elongational flow that occurs around the gate area. Such a behavior is not considered in the simulation since the elastic strain tensor was calculated based on a shear flow alone. In addition, the predicted normal birefringence of PC OQ3820 is lower at lower injection speeds than that in the measurements. This may be also due to the calculated pressure that is being lower than the measured pressure during cavity filling, since the injection speed was not strictly constant, as shown in Fig. 7b.

Fig. 17b displays a comparison of the measured and predicted normal birefringence, $<\Delta n_{13}>$, along the flow direction at different packing pressures for LGP moldings of PC OQ1030 and PC OQ3820 obtained in Runs #4, 1 and 5. The normal birefringence increases with increasing packing pressure in LGP moldings of both PCs. However, the effect is seen to be less significant in PC OQ1030. This may be due to a lower viscosity and molecular weight of PC OQ1030 exhibiting a lower relaxation time accelerating the relaxation process. Simulations are in a qualitative agreement with experimental data, but they are not able to describe correctly the shape of normal birefringence curves near the gate.

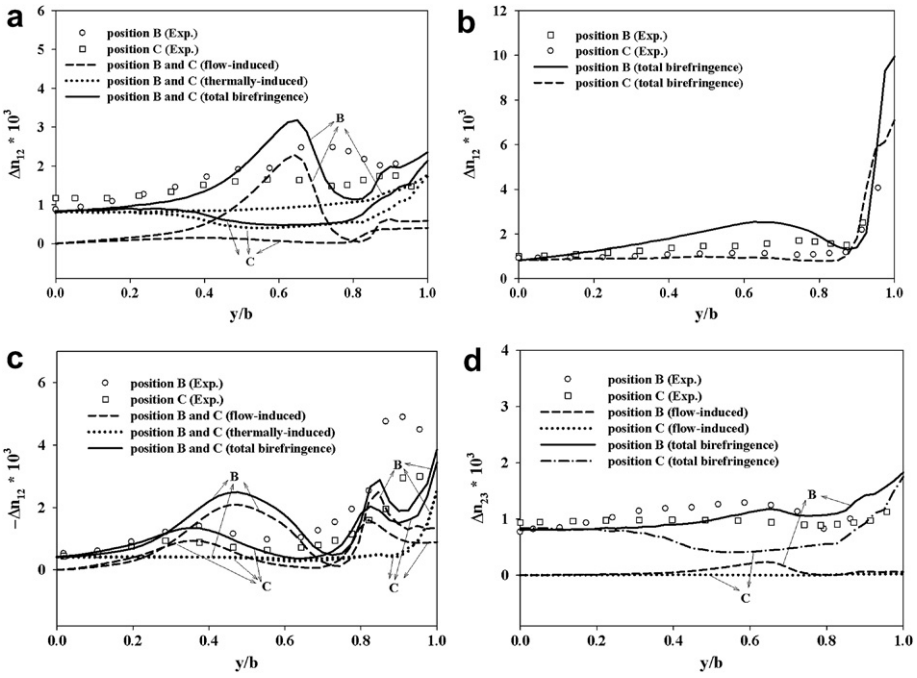


**Fig. 16.** Comparison of the gapwise distribution of the measured residual birefringence (symbols) and calculated residual flow-, thermally-induced and total birefringence of $\Delta n_{12}$ for PC OQ1030 (a), PC OQ3820 (b), PS 615 (c) and $\Delta n_{23}$ for PC OQ1030 (d) at locations B and C in LGP moldings obtained in Run #1.

Fig. 17c exhibits a comparison of the measured and predicted normal birefringence, $<\Delta n_{13}>$, along the flow direction at different packing times for LGP moldings of PC OQ1030 and PC OQ3820 obtained in Runs #6, 1 and 7. The measured and predicted normal birefringence shows a minor effect of the packing time. It was found that at processing condition of Run #1, the gate freezes off at time of 2.16 and 2.54 s for PC OQ1030 and PC OQ3820, respectively. The shortest packing time used in experiment is 2 s which is close to gate freezing time. When the gate freezes, the development of birefringence is dominated by relaxation process. Accordingly, the predicted normal birefringence is very little affected by the variation of the packing time. It should be noted that this observation is contrary to earlier observation in molding of PC disk [19], where it was shown that the normal retardation near the cavity entrance increased significantly with the packing time. This difference between the normal birefringence behavior in LGP moldings of the present study and disk moldings of earlier study [19] is due to the difference in gate thickness. The gate was thicker in the PC disk mold requiring much longer time for its freezing, therefore allowing a more melt to enter the cavity during the packing stage at a longer packing time.

Fig. 17d depicts a comparison of the measured and predicted normal birefringence, $<\Delta n_{13}>$, along the flow direction at different mold temperatures for LGP moldings of PC OQ1030 and PC OQ3820 obtained in Runs #8, 1 and 11. Experiments and simulations show that the normal birefringence increases with reducing mold temperature. LGP moldings of PC OQ1030 show a dominating effect of relaxation process at locations further away from the gate where the normal birefringence is not affected by the mold temperature. But such phenomenon is not observed in PC OQ3820. Although the predictions show a qualitative agreement with experimental data, a noticeable deviation is observed in Run #8 of PC OQ3820. This may be due to the increased contribution of the elongational stresses in the gate region caused by a lower mold temperature resulting in an increase of the cooling rate and therefore relaxation time retarding the stress relaxation.

Fig. 17e demonstrates a comparison of the measured and predicted normal birefringence, $<\Delta n_{13}>$, along the flow direction at different melt temperatures for LGP moldings of PC OQ1030 and PC OQ3820 in Runs #9, 1 and 10. The normal birefringence reduces with increasing melt temperature, but the effect is not as strong as the effects of the packing pressure and mold temperature. LGP moldings of both PCs show minor changes in the normal birefringence at locations further away from the gate due to a dominating effect of the relaxation process. In Fig. 17e, predictions are in a fair agreement with measurements at locations further than 4 mm away the gate. However, more deviations are found near the gate where the normal birefringence exhibits a maximum. In Fig. 17e, the measured normal birefringence in LGP molding of PC OQ3820 in Run #10 corresponding to the highest melt temperature indicates a formation of maximum which is not observed at lower melt temperatures corresponding to Runs #1 and 9. It seems like that a lower viscosity at a high melt temperature causes the appearance of this maximum. Also, the predictions at higher melt temperatures (Runs # 1 and 10) show a better agreement with experimental data at locations further away from the position of the maximum.

Fig. 18 exhibits a comparison of the measured and predicted normal birefringence, $<\Delta n_{13}>$, along the flow direction at different processing conditions for LGP moldings of PS obtained in Runs #1, 2 and 3 (Table 3). The normal birefringence is negative and reduces with increasing melt temperature and reducing packing time. Similar to LGP moldings of PCs, the effect of the melt temperature on the normal birefringence is not significant. However, in contrast to LGP moldings of PCs, the packing time significantly affects the development of the normal birefringence in case of PS. This is due to the gate freezing time of PS being significantly higher than that of both PCs. In fact, according to simulations, the gate freezing time for PS in Run #1 is 3.35 s in contrast to 2.16 s and 2.54 s at Run #1 for PC OQ1030 and PC OQ3820, respectively. This indicates the cooling rate of PS is considerably lower than that of both PCs. Also, even though the PS 615 has much higher value of the stress-optical coefficient in the melt state, compared to the PC OQ3820, the

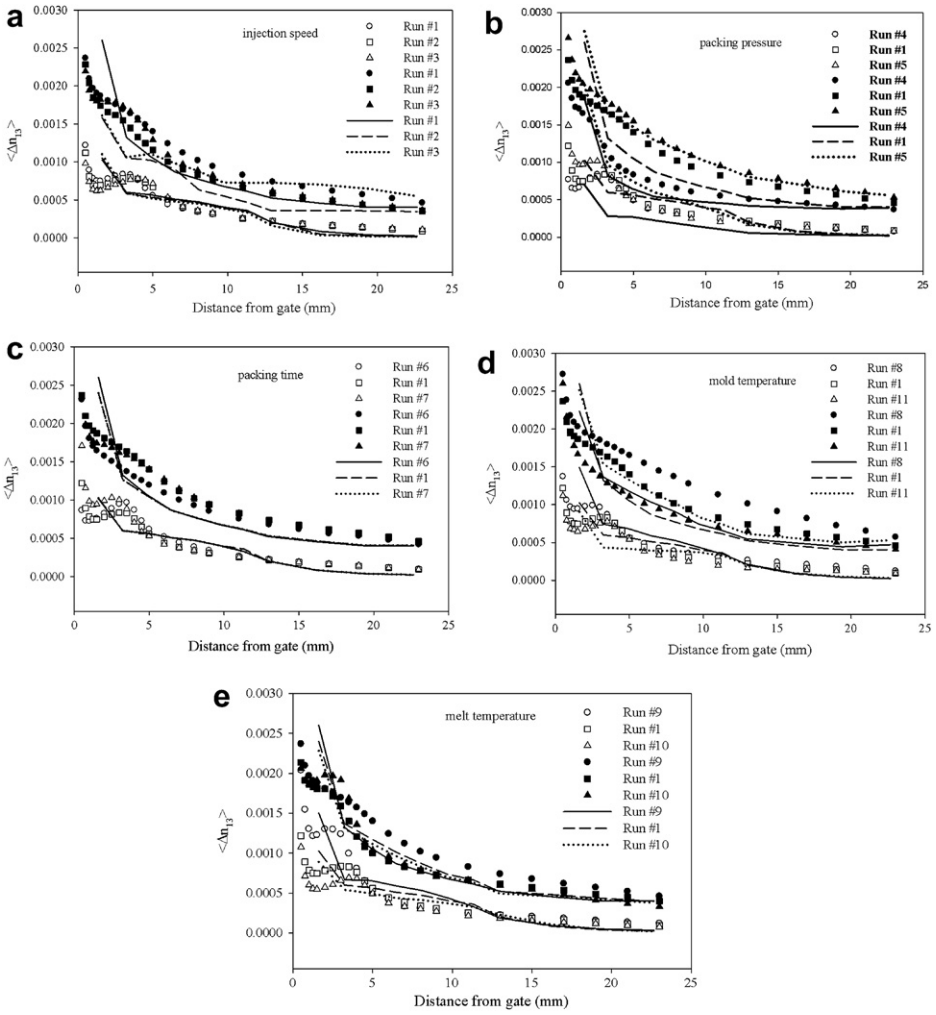


**Fig. 17.** The measured (symbols) and simulated (curves) gapwise averaged normal birefringence component $<\Delta n_{13}>$ along the flow direction at various processing conditions in LGP moldings of PC OQ1030 (open symbols) and PC OQ3820 (filled symbols).

normal birefringence of LGP moldings of this PC is similar or higher than that of PS 615. This is due to a faster cooling retarding the relaxation process during molding of PC OQ3820.

Fig. 19 shows the averaged measured luminance as a function of the measured averaged normal birefringence. The luminance was averaged for the angle of rotation of LGP within −20 to +20 degrees. The normal birefringence was averaged along the width direction of LGP moldings of PC OQ1030 and PC OQ3820. The measurement of luminance of various LGP moldings was reported in Ref. [9] where a correlation between the luminance and the degree of filling of V-grooves in LGP moldings was presented. In the present study, the normal birefringence in LGP moldings for all processing conditions is measured and presented in Fig. 19. Clearly, a correlation exists between the frozen-in normal birefringence and the luminance of LGP moldings. In particular, the luminance depends on the molecular weight of PC with the higher molecular weight leading to a lower luminance, as shown by two sets of data. The lower luminance of LGP moldings is due to the higher frozen-in normal birefringence.

### 3.4.5. Anisotropic shrinkage

Anisotropic shrinkage including the length, width and thickness shrinkages of moldings results from anisotropy of molecular

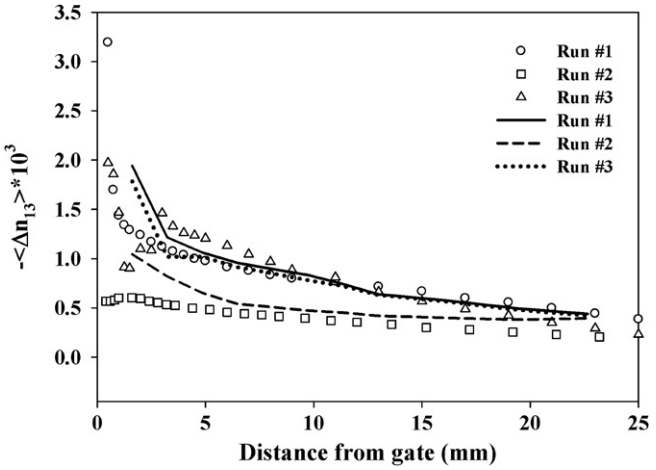


**Fig. 18.** Measured (symbols) and predicted (curves) gapwise averaged normal birefringence component $<\Delta n_{13}>$ along the flow direction at different processing conditions in LGP moldings for PS 615.

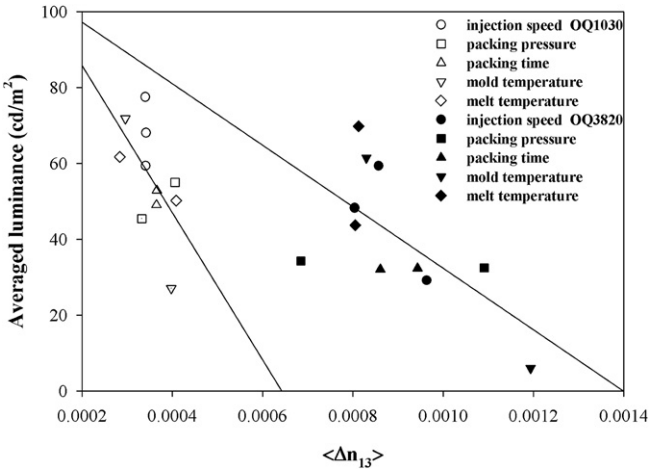


**Fig. 19.** Average luminance as a function of average normal birefringence for LGPs of PC OQ1030 (open symbols) and PC OQ3820 (filled symbols) obtained at various processing conditions.

orientation. For amorphous polymers, such shrinkage development is influenced by the volumetric shrinkage, flow-induced orientation and heat transfer during the molding process. Fig. 20 shows the measured and predicted length, width and thickness shrinkage as a function of injection speed (a), packing pressure (b), packing time (c), mold temperature (d) and melt temperature (e) in LGP moldings of PC OQ1030 and PC OQ3820. In particular, Fig. 20a indicates a comparison of three shrinkages as a function of the injection speed for PC OQ1030 and PC OQ3820. Among various shrinkages, the thickness shrinkage in LGP moldings of both PCs shows the highest value. The thickness shrinkage seems to be only slightly affected by the injection speed. This is due to the fact that the shrinkage is mainly determined by the specific volume history during the packing stage while the injection speed is imposed before the packing stage and has only a limited influence on this stage. Also, a higher injection speed results in a higher local pressure lowering the value of specific volume at the end of the filling stage. However, at a higher injection speed, more viscous heating is also introduced, therefore leading to a higher value of specific volume at the end of the filling. Accordingly, the tendency of shrinkage variation with the injection speed is determined by a competition between an increase and decrease of the specific volume at the end of the filling stage due to variations of temperature and pressure. The LGP moldings of PC

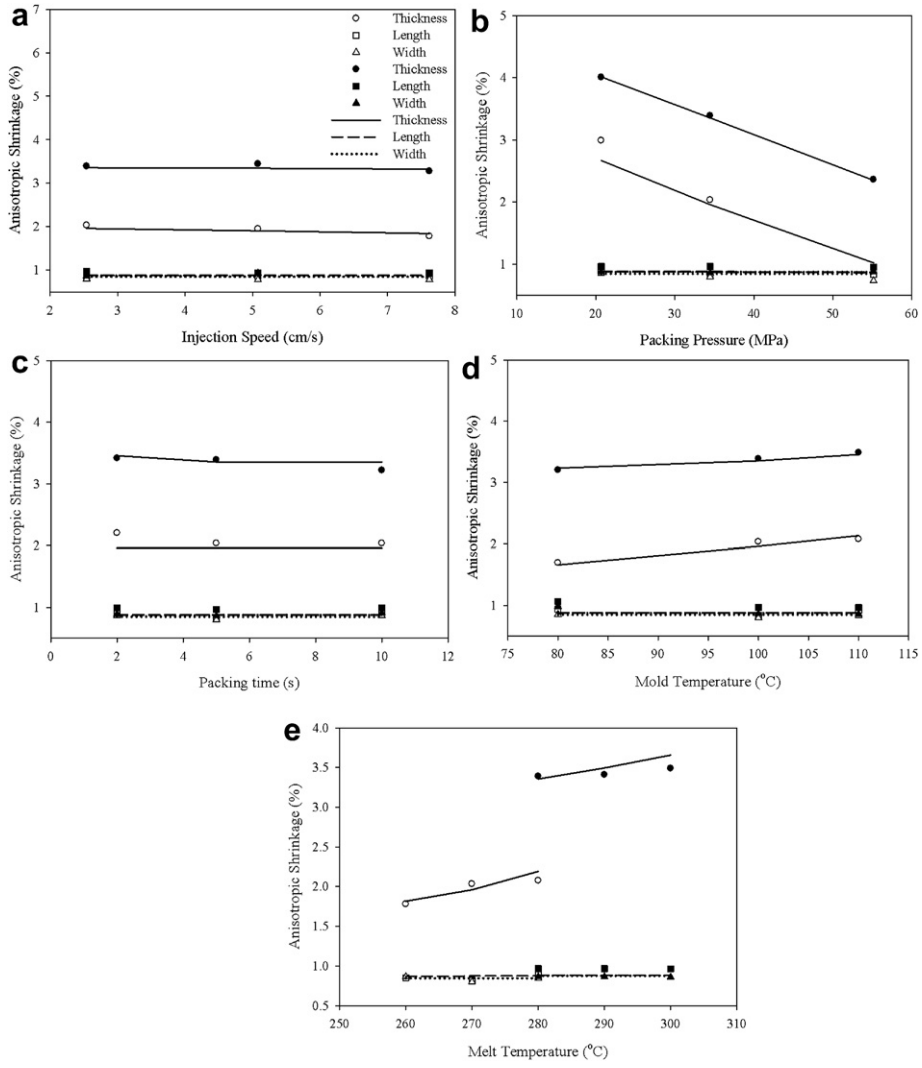


**Fig. 20.** The measured (symbols) and simulated (curves) shrinkage as a function of processing conditions in LGP moldings of PC1030 (open symbols) and PC3820 (filled symbols).

OQ3820 display a higher value of shrinkage in all directions than that of PC OQ1030. The difference between the length and width shrinkages (in the plane shrinkages) is insignificant, but the width shrinkage is slightly lower than the length shrinkage. This is due to a low level of molecular orientation introduced in moldings of amorphous polymers. The measured and simulated shrinkages are in good agreement.

Fig. 20b indicates a variation of anisotropic shrinkages with the packing pressure in LGP moldings of PC OQ1030 and PC OQ3820. The thickness shrinkage is reduced by increasing packing pressure, as indicated by both measurements and simulations. The predicted anisotropic shrinkage indicates a good agreement with measurements in LGP moldings of both PCs. However, PC OQ3820 displays a higher value of shrinkage in every direction than PC OQ1030, although their PVT behaviors are the same. This is because a higher viscosity PC OQ3820 introduces a higher viscous heating. Also, the melt temperature used in PC OQ3820 was 10 °C higher than that in PC OQ1030.

Fig. 20c indicates anisotropic shrinkages as a function of the packing time in LGP moldings of PC OQ1030 and PC OQ3820. Measurements and simulations show a very little variation of all shrinkages in LGP moldings with the packing time. In earlier study [26], the packing time was found to be the most significant factor in the development of shrinkage of a PS strip. This contradiction cannot be explained by a higher thermal conductivity of PC over that of PS (see Table 1), introducing a higher cooling rate during molding. The gate is thin (0.82 mm) in the LGP mold. That means the gate freezes relatively faster than that in the strip cavity having the gate thickness of 3.18 mm [26]. In fact, it was found that the gate freezes off at 2.16 and 2.54 s for PC OQ1030 and PC OQ3820, respectively, according to the simulation at processing conditions of Run #1. In PS strip cavity [26] the gate was thick and therefore it freezes at later time allowing for more melt to be pushed into the cavity during the packing stage. In case of LGP moldings during the packing stage, an additional melt cannot be forced into the cavity after gate freezes to compensate for the shrinkage. That explains the contradiction of why the shrinkage is not affected by the packing time in the present study. Actually, the LGP molding of PC OQ3820 at the packing time of 2 s shows a slightly higher shrinkage because the gate freezing time is slightly higher than the packing time.

Fig. 20d indicates anisotropic shrinkages as a function of the mold temperature for LGP moldings of PC OQ1030 and PC OQ3820. Again, the length and width shrinkages show limited variation due to a low level of the molecular orientation introduced in LGP moldings of amorphous polymers. The thickness shrinkage increases with increasing mold temperature. This is due to a slower cooling rate resulting in a hotter melt core with the specific volume being relatively higher compared to that of the lower mold temperature. Also, the slower cooling rate causes a faster pressure relaxation and results in a higher value of specific volume.

Fig. 20e indicates anisotropic shrinkages as a function of the melt temperature for LGP molding of PC OQ1030 and PC OQ3820, respectively. Again, the length and width shrinkages show a minor variation due to a low level of the molecular orientation. The thickness shrinkage increases with increasing melt temperature. From comparison of Fig. 20d and e, it is clear that the melt temperature has more significant effect on the thickness shrinkage than the mold temperature at the increment of temperature variations in this study. The thickness shrinkage of LGP moldings of PC OQ3820 is higher than that of PC OQ1030 due to a higher melt temperature applied and more viscous heating introduced in case of PC OQ3820. Also, it is more difficult to push higher viscosity PC OQ3820 into the cavity.

Fig. 21 shows a comparison of anisotropic shrinkages at different processing conditions for LGP moldings of PS 615. The length shrinkage is slightly higher than the width shrinkage as observed on both PCs. A minor variation of in-plane shrinkages is shown by varying processing conditions indicating a low level of the molecular orientation. Also, the thickness shrinkage slightly increases with increasing melt temperature and significantly increases with reducing packing time. The difference of the influence of the packing time on the thickness shrinkage in case of LGP moldings of PS in comparison with those of both PCs is due to a longer gate freezing time in case of PS. The predicted thickness shrinkage at the processing condition of Run #2 is higher than the measured shrinkage. However, the reason for this discrepancy is not clear at this point.

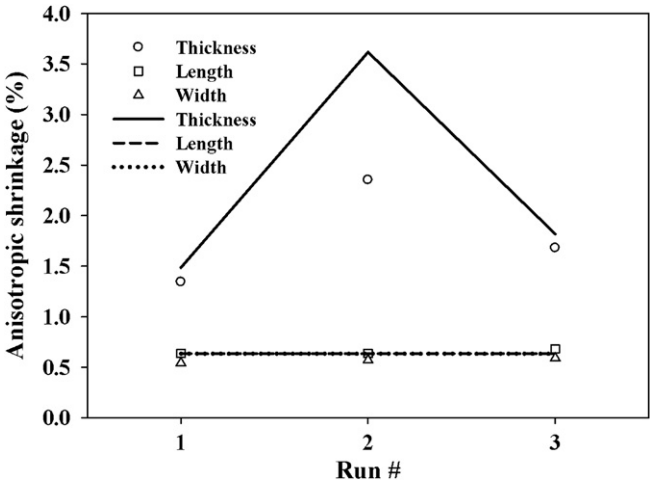


**Fig. 21.** The measured (symbols) and simulated (lines) anisotropic shrinkages as a function of processing conditions in LGP moldings of PS 615.

## 4. Conclusions

Numerical simulations of the thermal, transverse and normal birefringence components and anisotropic shrinkages in LGP moldings are carried out based on viscoelastic and photo-viscoelastic constitutive equations. Simulations are performed using a combination of a CV/FE/FD techniques described in Part I [11]. The molding experiments were performed and the pressure development during LGP molding, transverse and normal birefringence components and anisotropic shrinkages in LGP moldings of two PCs and PS 615 were measured. The simulated data were compared with experimental results. The effect of various processing conditions on the development of the normal birefringence in LGP moldings of PCs is ranked from most to least: the packing pressure, mold temperature, melt temperature, injection speed and packing time. However, in LGP moldings of PS 615 the packing time is found to be a significant factor due to a longer gate freezing time. LGP moldings of both PCs show not only different levels of the normal birefringence, but also dissimilar patterns. A higher value of the normal birefringence in LGP moldings of PC OQ3820 in comparison with those of PC OQ1030 is observed due to a higher stress-optical coefficient of PC OQ3820 and also higher normal and shear stresses achieved during the cavity filling due to its higher viscosity in comparison with that of PC OQ1030. It is found that simulations are in fair agreement with experiments concerning the level of the residual normal birefringence but are unable to describe the exact shape of measured curves, especially the formation of a maximum of the normal birefringence at locations close to the gate. The latter is due to the elongational flow in the gate area [25], which is neglected in the present simulations. An inclusion of

nonisothermal contraction and expansion flows in the gate area is required to find contributions of the elongational flow.

Without inclusion of the thermally-induced birefringence, the simulated transverse residual flow birefringence components $\Delta n_{12}$ and $\Delta n_{23}$ in LGP moldings is significantly lower than the measured transverse birefringence components. The thermally-induced birefringence arises due to rapid cooling effects in the thickness direction of LGP moldings. To understand the effect of processing conditions on the flow-induced birefringence, simulations of birefringence components $\Delta n_{12}$ and $\Delta n_{23}$ were carried out at various processing conditions including the injection speed, packing pressure, packing time, melt temperature and mold temperature. Birefringence of LGP moldings of both PCs and a PS exhibit distinct gapwise distribution patterns in the development of $\Delta n_{12}$ and $\Delta n_{23}$. LGP moldings of PC OQ1030 indicate a highly pronounced maximum of these components further away from the wall than that of PC OQ3820. However, LGP moldings of PC OQ3820 exhibit a higher residual flow-induced birefringence near the wall than that of PC OQ1030. This is due to low viscosity of PC OQ1030 leading to a faster relaxation process. It is concluded that the viscosity and relaxation time of melts play important roles on how the processing conditions affect the development of the residual flow-induced transverse birefringence.

The thermally-induced birefringence in LGP moldings is calculated by a combination of constrained and free quenching assumption for PCs and PS. The constrained and free cooling is, respectively, imposed during time period when the pressure is non-zero and zero. The pressure calculated from simulations is used to determine the time to switchover from constrained to free cooling. The thermal birefringence in LGP moldings of PCs varies with location in the mold due to a longer duration of constraint, while the thermal birefringence in LGP moldings of PS is not affected by location in the mold since the duration of constrained cooling is short. It indicates that the moment of release of constraint is an important factor in the development of the thermally-induced birefringence. In fact, the thermally-induced birefringence will be a constant through the thickness, if the constrained condition is maintained until thermal equilibrium is achieved. In LGP moldings of PCs, the thermally-induced birefringence is nearly constant in the core region and increases in the wall region.

The calculated thermally-induced birefringence was added to the flow-induced birefringence to obtain the total frozen-in transverse birefringence in LGP moldings. In LGP moldings of PS and PCs, the thermal birefringence provides, respectively, minor and major contributions to the total birefringence compared to that of the flow-induced birefringence. It is also found that the birefringence component $\Delta n_{23}$ is mainly determined by the thermally-induced birefringence since the flow in the direction of 3 is weaker than that in direction of 1. With inclusion of the thermal birefringence the gapwise distribution of the simulated total birefringence was close to the measured one.

Numerical simulations of anisotropic shrinkages in LGP moldings of PCs and PS at various processing conditions are carried out and the results are compared with measurements. A good agreement between the simulated and measured anisotropic shrinkages at various processing conditions was obtained. LGP moldings of both PCs show similar tendencies in the variation of shrinkages with processing conditions. However, a higher value of shrinkage in LGP moldings of PC OQ3820 was observed due to its higher viscosity. It is concluded that the shrinkage in moldings of amorphous polymers is influenced by the volumetric shrinkage, flow-induced residual birefringence and heat transfer during the molding process, especially in the packing stage. The gate freezing time is observed to be an important factor in the development of shrinkages. The effect of processing conditions on the development of shrinkages in LGP moldings of PCs is ranked from most to least: the packing pressure, melt temperature, mold temperature, injection speed and packing time. In LGP moldings of PS, the thickness shrinkage slightly increases with increasing melt temperature and significantly increases with reducing packing time. The latter was due to a longer gate freezing time in PS. Anisotropic shrinkages obtained at different processing conditions indicated that there is coupling effects of multiple factors affecting shrinkages including processing variables, mold and polymer with the temperature and pressure histories being most defining factors.

## Acknowledgement

The authors greatly appreciate the financial support of the NSF Division of Engineering under grant DMI-0322920.

## References

[1] Greener J, Wiberger-Friedl R, editors. Precision injection molding: process, materials and applications. Munich: Hanser; 2006.
[2] Kamal MR, Isayev AI, Liu SJ, editors. Injection molding: technology and fundamentals. Munich: Hanser; 2009.
[3] Togaya A, Nagai M, Koike Y, Yokohama K. Thin liquid–crystal display backlight system with highly scattering optical transmission polymers. Appl Opt 2001;40:6274–80.
[4] Okumura T, Tagaya A, Koike Y. Highly-efficient backlight for liquid crystal display having no optical films. Appl Phys Lett 2003;83(13):2515–7.
[5] Visser RJ. Application of polymer light-emitting materials in light-emitting diodes, backlights and displays. Philips J Res 1998;51:467–77.
[6] Feng D, Jin G, Yan Y, Fan S. High quality light guide plates that can control the illuminance angle based on microprism structures. Appl Phys Lett 2004;85:6016–8.
[7] Feng D, Yan Y, Yang X, Jin G, Fan S. Novel integrated light-guide plates for liquid crystal display backlight. J Opt A: Pure Appl Opt 2005;7:111–7.
[8] Han X, Yokoi H, Takahashi T. Effects of cavity conditions on transcription molding of microscale prism patterns using ultra-high speed injection molding. Intern Polym Process 2006;XXI(5):473–9.
[9] Lin TH, Isayev AI, Mehranpour M. Luminance of injection molded V-groove light guide plates. Polym Eng Sci 2008;48(8):1615–23.
[10] Lee JG, Lee BK, Kang TG, Kwon TH. Experimental and theoretical investigation of injection molding with microrib patterns. Polym Eng Sci 2010;50:1186–98.
[11] Isayev AI, Lin TH. Frozen-in birefringence and anisotropic shrinkage in optical moldings: I. Theory and simulation scheme. Polymer 2010;51(1):316–27.
[12] Leonov AI. Nonequilibrium thermodynamics and rheology of viscoelastic polymer media. Rheol Acta 1976;15:85–98.
[13] Janeschitz-Kriegl H. Polymer melt rheology and flow birefringence. New York: Springer; 1983.
[14] Ames WF. Numerical methods for partial differential equations. 3rd ed. Boston: Academic Press; 1992.
[15] Shyu GD, Isayev AI, Li CT. Photoviscoelastic behavior of amorphous polymers during transition from the glassy to rubbery state. J Polym Sci Phys Ed 2001;39:252–2262.
[16] Shyu GD, Isayev AI, Li CT. Residual thermal birefringence in freely quenched plates of amorphous polymers: simulation and experiment. J Polym Sci Phys Ed 2003;41:1850–67.
[17] Press WH, Teukolsky SA, Vetterling WT, Flannery BP. Numerical recipes in FORTRAN: the art of scientific computing. 2nd ed. Cambridge University Press; 1992.
[18] MOLDFLOW data base, Version 6. Moldflow, Framingham, MA, 2006.
[19] Isayev AI, Shyu GD, Li CT. Residual stresses and birefringence in injection molding of amorphous polymers. J Polym Sci Polym Phys 2006;44(3):622–39.
[20] Brandrup J, Immergut EH. Polymer handbook. 3rd ed. New York: Wiley-Interscience; 1989.
[21] Lin TH, Isayev AI. Photoviscoelastic behavior and residual thermal birefringence in optical grade polycarbonates. Rheol Acta 2008;47:977–88.
[22] Wang KK, Cohen C, Koch DL, Hieber CA, Yoon K, Gupta M, et al. Cornell injection molding program progress report No.16. Ithaca, New York: Cornell University; 1991.
[23] Randy JN. An introduction to the finite element method. 2nd ed. New York: McGraw-Hill; 1993.
[24] Ghoneim H, Hieber CA. Incorporation of density relaxation in the analysis of residual stresses in molded parts. Polym Eng Sci 1997;37:219–27.
[25] Isayev AI, editor. Injection and compression molding fundamentals. New York: Marcel Dekker, Inc.; 1987.
[26] Kwon K, Isayev AI, Kim KH. Toward a viscoelastic modeling of anisotropic shrinkage in injection molding of amorphous polymers. J Appl Polym Sci 2005;98:2300–13.